Check for updates

Breaking through the thick-electrode barrier: rational design for high-loading Zn–MnO₂ batteries

Qingyang Yin, [ID] [a] Wenqing Lu [ID] *[a] and Zheng Chen [ID] *[a,b]

Zn–MnO₂ batteries hold great promise for grid-scale and stationary energy storage applications. Their inherently low cost, safety, and environmental benignity make them ideally suited for gigaton-level energy storage. In recent years, research focus has increasingly shifted toward achieving high areal capacity and energy density, aiming to uncover practically relevant insights for their real-world deployment. However, significant challenges emerge when employing MnO₂ electrodes at elevated areal loadings. In this review, we identify the thick-electrode barrier, encompassing issues that stem from intrinsic material properties and reaction mechanisms, as well as limitations imposed by high-loading electrode configurations. We further provide a comprehensive summary of recent advances toward realizing high areal-capacity Zn–MnO₂ batteries. By connecting fundamental understanding with practical design principles, this review aims to offer guidance for overcoming the thick-electrode barrier and accelerating the practical implementation of Zn–MnO₂ batteries for sustainable energy storage.

Broader context

Grid-scale stationary energy storage demands solutions that combine low cost with environmental sustainability. Leveraging their resource abundance, intrinsic safety, and favorable energy density, Zn-based batteries have become attractive targets. Among them, interest in the Zn–MnO₂ chemistry has re-emerged, shifting from traditional alkaline primary cells to mildly acidic rechargeable systems to improve reversibility and lifetime. This review examines the opportunities and challenges of Zn–MnO₂ batteries, with a special emphasis on high-loading configurations that are closely tied to practical demonstration and deployment. By surveying recent advances across materials, architectures, and electrolytes, we aim to clarify the barriers to high-loading configurations and to outline pathways toward competitive levelized cost of storage for long-duration energy storage.

1. Introduction

Grid-scale energy storage is vital to advancing and stabilizing modern power systems as they transition to cleaner energy sources. Long-duration energy storage (LDES), typically defined as systems capable of providing ten or more hours of discharge, is critical for diverse clean-energy and resilience applications.[1,2] Although Li-ion batteries are currently dominating the energy storage market, their flammable electrolytes, narrow safety margins, and reliance on scarce critical materials (*e.g.*, Li, Co, Ni) constrain scalability and limit long-term viability for grid-scale deployment.[3,4]

These limitations have spurred interest in alternative chemistries that combine safety, cost-effectiveness, and environmental sustainability. Among emerging options, aqueous rechargeable batteries, which use water-based electrolytes, stand out for their intrinsic safety, low cost, and benign environmental profile.[5–8] When paired with inexpensive Zn metal anodes, aqueous Zn-ion batteries (AZIBs) offer a particularly attractive pathway toward practical, large-scale energy storage.[9–11] As shown in Fig. 1a, we benchmark Zn-based batteries against other energy storage chemistries from a system-level perspective. The initial capital cost, round-trip efficiency, and storage duration are critical parameters because they directly determine the levelized cost of storage (LCOS), defined as the average price per unit of discharged energy required to recover all capital and operating expenses over the system's lifetime.[12] Environmental impact is likewise essential for sustainable, large-scale deployment in LDES.

Specifically, conventional lead–acid batteries, although commercially mature and low cost, suffer from poor cycle life and low efficiency, which leads to unfavorable LCOS values.[13] In addition, the use of toxic lead components raises serious environmental and safety concerns. By contrast, Li-ion bat-

[a]Aiiso Yufeng Li Family Department of Chemical and Nano Engineering, University of California, San Diego, La Jolla, CA 92093, USA. E-mail: zhc199@ucsd.edu, wel100@ucsd.edu
[b]Sustainable Power and Energy Center, University of California, San Diego, La Jolla, CA 92093, USA
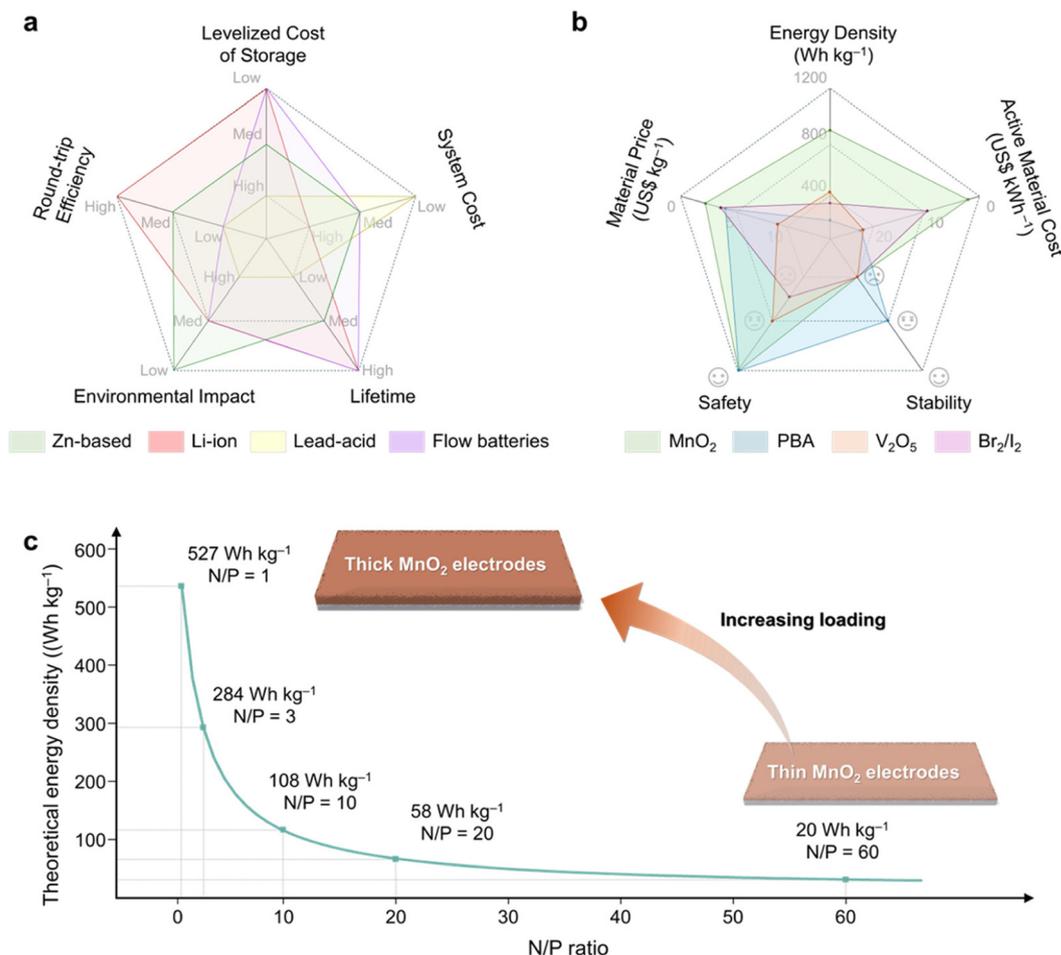
Fig. 1 (a) Comparison of representative battery technologies in terms of LCOS, initial capital cost, round-trip efficiency, lifetime, and environmental impact. (b) Comparison of cathode materials for AZIBs in terms of theoretical energy density, raw material price, active-material cost per kWh, cycling stability, and safety. (c) Theoretical energy density of Zn–MnO$_2$ batteries at different N/P ratios, calculated based on the mass of active materials in the cathode and anode.

teries and flow batteries such as vanadium redox flow batteries (VRFBs) deliver high round-trip efficiency and long lifetimes, resulting in low LCOS values even at elevated costs.[13,14] State-of-the-art AZIBs currently occupy a middle ground: despite intrinsically low material cost and a benign environmental profile, their moderate round-trip efficiency and limited cycle life yield medium LCOS values, still falling short of the \$0.05 per kWh target for LDES.[15]

To pursue a lower LCOS for LDES, future AZIBs should prioritize chemistries that improve performance, particularly efficiency and cycling stability, while preserving low cost and low environmental impact. To this end, we compare representative AZIB cathodes to assess cost-performance trade-offs (Fig. 1b and Table 1). Specifically, vanadium pentoxide (V$_2$O$_5$) offers a theoretical capacity of 589 mAh g^{-1} but operates at a low average discharge voltage (~0.6–0.8 V vs. Zn/Zn^{2+}), yielding a modest energy density of 412 Wh kg^{-1}. Coupled with its high raw-material cost (US\$ per 8.99 kg), V$_2$O$_5$ exhibits active-material costs of US\$ 21.8 per kWh.[16–18] Prussian blue analogs (PBAs) typically deliver lower specific capacities (~170 mAh

Table 1 Comparison of representative cathode materials in terms of theoretical specific capacity, estimated energy density, and raw material cost. Raw material prices are sourced from the Shanghai Metals Market (2025) and the United States Geological Survey (2024–2025). All energy density and materials cost values are calculated based on the mass and raw material cost of the cathode active material only. Inactive components such as binders, conductive additives, current collectors, and electrolyte are not included

Battery chemistry	Specific capacity (mAh g^{-1})	Cathode material price (US\$ per kg)	Energy density (Wh kg^{-1})	Active material cost (US\$ per kWh)
Zn–MnO$_2$	617	2.08	926	2.2
Zn–V$_2$O$_5$	589	8.99	412	21.8
Zn–PBA	170	3.84	170	22.6
Zn–Br$_2$	220	3.30	352	9.4
Zn–I$_2$	211	59.00	211	279.6

g^{-1}), resulting in similarly high active-material costs (US\$ 22.6 per kWh).[19–22] Halogen-based cathodes such as Br$_2$ and I$_2$ show moderate capacities but face challenges such as shuttle

effects and volatility, and in the case of I_2, a prohibitively high raw-material price (US\$ 279.6 per kWh).[23,24] Because active-material cost per kWh represents the minimum possible contribution of the active material to system-level costs, it provides a critical baseline for assessing economic feasibility: even with low balance-of-system costs, expensive or low-energy-density cathodes can dominate the total cost structure.

MnO$_2$ stands out among all candidates with its high theoretical capacity (617 mAh g^{-1}, two-electron reaction), favorable operating voltage (>1.2 V), and exceptionally low raw-material price (US\$ 2.08 per kg), resulting in the lowest material cost of only US\$ 2.2 per kWh.[25–27] Furthermore, MnO$_2$ is earth-abundant, non-toxic, and environmentally benign, making it highly attractive for grid-scale and stationary storage applications where cost, safety, and sustainability are paramount.[28–32] To fully exploit these advantages for achieving low LCOS in LDES, recent research has shifted toward mildly acidic electrolytes to improve cycle life, coulombic efficiency, and lifetime energy throughput. Unlike in alkaline systems, where Mn dissolution and passivation layer growth severely limit reversibility,[11] acidic electrolytes stabilize Mn redox reactions, suppress dendrites, and enable efficient Zn plating/stripping.[33] These improvements in cycling stability and round-trip efficiency increase the total energy delivered per unit cost and thereby lower LCOS toward the LDES target.

Despite these advances, however, most reported Zn–MnO$_2$ configurations remain far from practical relevance. To illustrate how cell configuration and areal capacity affect system-level metrics, we calculated the theoretical energy density of Zn–MnO$_2$ cells at different negative-to-positive capacity ratios (N/P ratios) using:

$$\varepsilon = \frac{Q \times V_{mid}}{m_{cathode} + m_{anode}} = \frac{Q \times V_{mid}}{\dfrac{Q}{q_{cathode}} + \dfrac{r_{N/P} \times Q}{q_{anode}}} = \frac{q_{anode} \times V_{mid}}{r_{N/P} + \dfrac{q_{anode}}{q_{cathode}}}$$

where ε is the theoretical energy density based on active materials, Q the capacity, V_{mid} the mid-voltage, $m_{cathode}$ and m_{anode} the mass of active materials in cathode and anode, respectively, $r_{N/P}$ the N/P ratio, and $q_{cathode}$ and q_{anode} the theoretical specific capacity of active materials in cathode and anode, respectively.

As shown in Fig. 1c, many reported systems employ thick Zn foils (~100 μm, ~58.5 mAh cm^{-2}) paired with low-loading MnO$_2$ cathodes (1–2 mg cm^{-2}, <0.5 mAh cm^{-2}). While such asymmetric designs can achieve tens of thousands of cycles, they suffer from high N/P ratios and low energy densities, ultimately reducing the delivered energy per unit cost and dominating the total cost structure, as discussed above. Achieving high MnO$_2$ areal loading, balanced N/P ratios, and lean electrolyte conditions is therefore essential for realizing commercially viable energy density and cost-effectiveness.[34–37]

Collectively, these analyses identify MnO$_2$ as a uniquely competitive cathode for AZIBs by combining high capacity, low cost, safety, and scalability. The remaining challenge, as well as the central focus of this review, is to develop high areal-loading MnO$_2$ electrodes that can translate these intrinsic advantages into practical, low-LCOS energy storage systems. To this end, we identify the key challenges associated with thick-electrode configurations from two perspectives: (i) the intrinsic material properties and reaction mechanisms of MnO$_2$ and (ii) the practical demands imposed by high mass-loading designs. This review systematically evaluates recent advances in thick MnO$_2$ electrodes, covering strategies such as interior (crystal structure) and exterior (surface) engineering of MnO$_2$, substrate modification, and electrolyte optimization. Throughout the review, we place particular emphasis on studies reporting areal capacities above 1 mAh cm^{-2}, preferably ≥5 mAh cm^{-2}, to examine how these strategies address the challenges specific to thick electrodes. We also highlight works demonstrating Ah-level pouch cell configurations with practical potential. Overall, our goal is to establish a comprehensive framework for the rational design of high-loading MnO$_2$ cathodes, enabling next-generation AZIBs to meet the advanced performance, cost, and safety requirements essential for grid-scale and stationary energy storage.

2. Roadblocks towards high-loading MnO$_2$ for practical AZIBs

2.1. Reaction mechanisms and corresponding challenges of MnO$_2$

During electrochemical cycling, MnO$_2$ cathodes can undergo multiple reaction pathways, including metal-ion intercalation, proton insertion, MnO$_2$/H$^+$ conversion, and MnO$_2$/Mn^{2+} dissolution/deposition.[27,38,39] These pathways govern the accessible specific capacity and energy density of the cathodes, as well as the cycle performance of the batteries As the dominant reaction mechanism depends on multiple factors such as MnO$_2$ crystallography, local pH, and electrolyte composition, considerable efforts have been devoted to elucidating the underlying mechanisms in aqueous battery systems.[40–43] Each reaction pathway also introduces distinct challenges (Fig. 2), and deeper insight into their intrinsic limitations is essential for developing materials-level guidelines to optimize MnO$_2$ cathodes for practical optimization.

2.1.1. Reaction _via_ intercalation and co-insertion. The crystal framework of MnO$_2$ can reversibly accommodate the insertion/extraction of multivalent cations such as Al^{3+},[44] Ca^{2+},[45] Zn^{2+},[46] Mg^{2+},[47] and Na$^+$.[48] The efficiency and stability of these processes are largely governed by the crystallographic characteristics of MnO$_2$, with tunnel-type and layered-type polymorphs exhibiting distinct electrochemical behaviors. Specifically, tunnel-type polymorphs (such as α-MnO$_2$, β-MnO$_2$, γ-MnO$_2$, and ε-MnO$_2$) comprise edge-sharing chains of [MnO$_6$] octahedra that link by corner sharing to form tunnel structures that accommodate cations and water molecules.[49] In contrast, layered δ-MnO$_2$ consists of edge-sharing [MnO$_6$] sheets with an open interlayer spacing of ~0.7 nm, which offers more accessible insertion sites and high ionic mobility.[50,51]
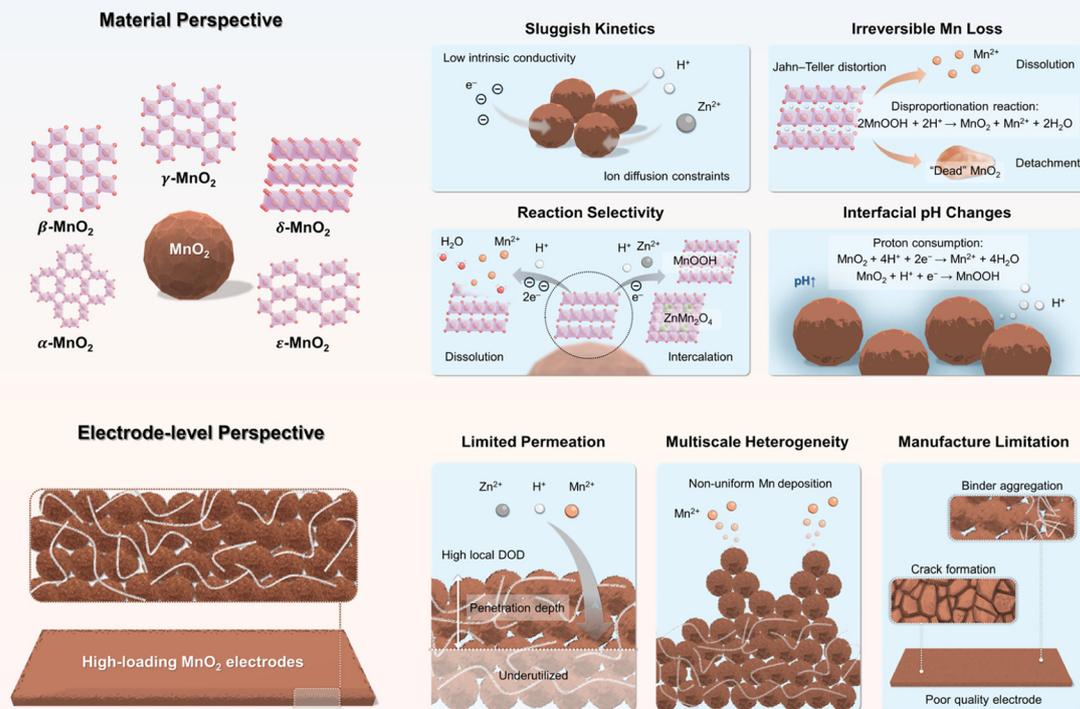
Fig. 2 Schematic illustration of the challenges limiting high areal loading MnO_2 cathodes in practical applications, highlighting issues arising from both reaction mechanisms and thick-electrode architecture.

Although the detailed working mechanisms remain under discussion, Zn^{2+}/H^+ co-insertion is broadly recognized as central across MnO_2 polymorphs, with both ions acting as reversible charge carriers.[27,52–55] While the co-intercalation can boost specific capacity *via* proton-coupled electron transfer (PCET), it also introduces several challenges. First, Zn^{2+} migrates more slowly than H^+ owing to its larger ionic size and stronger solvation shell. When both ions co-insert, the ensuing charge redistribution and local strain penalize long-range ion transport and electronic conductivity within MnO_2.[56,57] Coupled with the intrinsically low electronic conductivity of MnO_2, these effects suppress rate capability at high currents.[58] Second, the Zn^{2+}/H^+ co-insertion promotes structural transformations and Jahn–Teller lattice distortions, causing loss of crystallinity and phase heterogeneity that diminish reversibility.[59] Third, proton insertion facilitates MnOOH disproportionation in acidic media, leading to Mn^{2+} dissolution and re-precipitation of detached MnO_2, and the resulting loss of Mn inventory manifests as progressive capacity decay.[60] Collectively, these factors underlie the well-documented cycling instability of MnO_2 cathodes in mild or acidic electrolytes.

To overcome these obstacles, extensive efforts have focused on structural engineering and materials modification. Cation or anion doping can enlarge tunnel or interlayer spacings and tune the local redox environment, thereby facilitating ion diffusion, enhancing intercalation kinetics, and buffering insertion/extraction-induced stress.[61,62] Surface engineering offers a complementary route: ultrathin organic, inorganic, or hybrid coatings can not only reduce interfacial charge-transfer resistance but also preserve the MnO_2 morphology during cycling and suppress Mn dissolution into the electrolyte.[63,64] In particular, coatings that lower interfacial water activity can disfavor H^+-driven Mn^{3+} formation, while conformal oxide shells provide physical barriers that impede Mn dissolution and disproportionation.[65]

Beyond these established approaches, recent work has developed novel synthesis methods and the exploration of new MnO_2 polymorphs or derivatives. For example, Archer *et al.* showed that introducing water-soluble polymers during hydrothermal synthesis promotes the formation of δ-MnO_2 and β-MnO_2 with smaller particle sizes, higher specific surface areas, and water-rich interlayers, features that collectively enhance electrochemical performance.[53] Tang *et al.* developed a novel tunnel-type polymorph, *t*-MnO_2, with Mg^{2+} ions stabilizing a 3 × 3 tunnel framework capable of reversibly accommodating Zn^{2+}, H^+, and SO_4^{2-} anions, achieving a reversible capacity of 398 mAh g^{-1} at 0.2 A g^{-1} with an average discharge voltage of ~1.41 V.[54] In addition, Lu *et al.* utilized layered β-MnOOH, which is electrochemically converted into δ-MnO_2 during cycling, preserving a stable layered framework during

H$^+$ insertion.[55] This layer-to-layer structural evolution improves the structural stability and cycling performance.

2.1.2. Reaction *via* conversion and dissolution/deposition. Recently, the conversion mechanism between MnO$_2$ and H$^+$,[66] along with the MnO$_2$/Mn^{2+} dissolution/deposition process,[7,67,68] has attracted growing attention as a promising pathway for achieving higher energy density in aqueous batteries. Unlike the intercalation or co-insertion mechanism, which typically involves a single-electron transfer reaction, the dissolution/deposition mechanism enables a two-electron transfer process, theoretically delivering a much higher specific capacity approaching 617 mAh g^{-1}, and thus enhancing the overall energy density of the system.[69,70]

However, significant challenges remain owing to the limited understanding of reversible two-electron aqueous electroplating/stripping (E/S) of MnO$_2$. A central issue is the competition among surface adsorption, bulk ion insertion, and E/S under mild or near-neutral pH conditions.[71] Rationally biasing this partitioning toward dissolution/deposition is essential not only to approach the two-electron theoretical capacity of MnO$_2$ but also to mitigate proton-induced lattice deformation and Mn loss discussed above. Yet this reaction landscape remains underexplored as it is governed by a broad set of factors—from MnO$_2$ crystallography to the local electrolyte environment such as Zn^{2+}/Mn^{2+} activities, concentration, and pH value. For example, Lu *et al.* showed that under mildly acidic electrolytes, H$^+$ insertion instead of Zn^{2+} dominates charge storage in α-MnO$_2$.[31] Yu *et al.* revisited Zn–MnO$_2$ batteries and Al–MnO$_2$ batteries in mildly acidic electrolytes using cathode-free battery and supplying Mn^{2+} directly in the electrolyte.[36] They showed that full charge/discharge cycles proceeded entirely through reversible MnO$_2$/Mn^{2+} deposition/dissolution with sufficient Mn^{2+}.

Moreover, the PCET nature of MnO$_2$ redox drives interfacial pH excursions that are increasingly recognized as critical. During discharge, protons participate in both intercalation and conversion reactions. Their consumption alkalizes the cathode interface and raises the local pH, whereas the reverse processes during charge release H$^+$ and acidify it.[72,73] Biro *et al.* employed *in operando* pH tracking during cycling and revealed periodic pH fluctuations across different electrolytes. For the typical Zn–MnO$_2$ electrolyte (2 M ZnSO$_4$ + 0.5 M MnSO$_4$), a pronounced pH variation was observed during electrodeposition and dissolution, with the pH shifting from ~3.5 to ~4.5. Notably, this large pH change occurred even under conditions with a relatively large electrolyte volume and a small MnO$_2$ loading (~5 mg cm^{-2} MnO$_2$, corresponding to ~3.1 mAh cm^{-2}, and an electrolyte-to-capacity (E/C) ratio of ~0.8 mL mAh^{-1}).[73]

Without effective regulation, such pH swings can become substantial, redirecting reaction pathways and aggravating side reactions.[74] For example, Yang *et al.* showed that proton concentration critically affects MnO$_2$ dissolution/deposition chemistry. Sufficient proton availability (pH < 4) is necessary for MnO$_2$ dissolution, whereas in neutral electrolytes, only proton or Zn^{2+} intercalation occurs.[75] Conversely, excessively low pH

promotes disproportionation of Mn^{3+} in metastable MnOOH, causing irreversible Mn loss *via* isolated MnO$_2$ formation and thereby accelerating capacity decay. Consistently, Wong *et al.* observed a pH increase from 3.38 at the initial state to 5.41 after the first discharge in a conventional electrolyte (10 mg α-MnO$_2$ cathode in 5 mL of 2 M ZnSO$_4$ + 0.2 M MnSO$_4$). Notably, during the subsequent charging process, the pH initially stabilized at ~5.4 before dropping rapidly to ~3.57. This transient pH plateau was attributed to a balance between OH$^-$ consumption associated with Zn$_x$MnO(OH)$_2$ formation and OH$^-$ generation from zinc sulfate hydroxide (ZSH) formation.[76] Those effects are expected to be further amplified in AZIBs operated under lean-electrolyte conditions.

2.2. Challenges associated with high-loading electrode configurations

As discussed earlier, enabling the practical application of MnO$_2$ cathodes necessitates the development of high-loading electrodes to achieve the target energy density of 150 Wh kg^{-1}.[77] Despite increasing the amount of active material is essential for achieving competitive energy and power metrics, it simultaneously introduces a range of interrelated challenges not encountered in their thin-electrode counterparts (Fig. 2). In this section, we present our perspective on the key obstacles associated with the electrochemical operation and fabrication of thick MnO$_2$ electrodes.

2.2.1. Sluggish electrochemical kinetics. The inherently sluggish electrochemical kinetics of thick electrodes remains a major barrier to practical deployment in high-energy systems. To mitigate electronic transport limitations, conductive additives are incorporated to establish percolating networks that facilitate efficient electron transport across the electrode. By contrast, ionic transport is governed by the architecture of the porous network, where the electrolyte-filled voids enable ion migration to the active material.

Building on foundational work by Newman and co-workers,[78] Jansen *et al.* derived an analytical expression for the characteristic penetration depth L_d, which describes how far ions can effectively penetrate into an operating electrode:[79]

$$L_{d} = \frac{\varepsilon}{\tau} \times \frac{DC_0 F}{(1 - t_+)I}$$

where ε is the porosity, τ the tortuosity, D the intrinsic ion conductivity, C_0 the electrolyte salt concentration, F the Faraday's constant, t_+ the cation transference number, and I the applied current density.

This expression highlights three controlling factors for L_d and, by extension, the active material utilization in thick electrodes. First, the geometric characteristics of the electrode microstructure, the porosity ε and tortuosity τ, determine the effective ionic diffusivity, D_{eff}:[80]

$$D_{eff} = \frac{\varepsilon}{\tau} \times D$$

Here, tortuosity τ quantifies the complexity of the ion transport pathways and is defined as the ratio of the actual curved

path length through the pore network (L_{pore}) to the straight-line distance across the electrode ($L_{straight}$):

$$\tau = \frac{L_{pore}}{L_{straight}}$$

Second, electrolyte properties are critical: higher C_0, larger t_+, and greater D collectively increase L_d by enhancing ionic conductivity and reducing concentration polarization. Third, the applied current density directly opposes penetration. Higher I lowers L_d, making it harder for ions to traverse the full electrode thickness during cycling. Consequently, thick electrodes experience more severe transport limitations at high C-rates than thinner electrodes.[81]

When the electrode thickness L exceeds L_d, transport limitations produce inhomogeneous state of charge (SOC) and depth of discharge (DOD) profiles within the electrode.[82] Typically, the outer layers near the surface experience deeper cycling, while the interior becomes underutilized or even ionically isolated. Such uneven utilization accelerates local degradation, promotes mechanical and structural damage, and exacerbates capacity fade and electrolyte decomposition.

To quantify the impact of transport limitations on practical capacity, Lestriez *et al.* introduced accessible capacity Q_I:[83]

$$\frac{Q_I}{Q_0} = \frac{L_d}{L}$$

where Q_0 is the nominal specific capacity. This relationship emphasizes that, assuming sufficient electronic conductivity and negligible solid-state diffusion limits, the practical capacity of thick electrodes is directly constrained by ion transport. As L increases, Q_I scales with the ratio $\frac{L_d}{L}$. Consequently, simply increasing mass loading or thickness does not translate into proportionally higher areal capacity or energy output.[84] These insights underscore the need to optimize microstructural geometry, electrolyte formulation, and local current distribution—rather than simply increasing electrode thickness alone. Addressing these challenges is critical for realizing the full potential of thick electrodes in practical high-energy battery systems.

2.2.2. Multiscale heterogeneity. As discussed above, the redox pathway of MnO_2 is highly sensitive to the local chemical and electrochemical environment. Variations in concentration profiles, interfacial pH, and overpotential can steer MnO_2 along distinct reaction pathways, introducing reaction-driven heterogeneity that undermines long-term cycling stability. This problem is amplified in thick MnO_2 electrodes, where ionic transport limitations and steep concentration gradients intensify with increasing thickness and mass loading.[85] At the microscale, these constraints produce pronounced inhomogeneity in reaction kinetics and phase evolution across both depth and surface. In particular, fluctuations in the electric double layer (EDL) at the electrode–electrolyte interface alter the local distribution and speciation of Mn^{2+} and protons, thereby modulating nucleation and growth dynamics during MnO_2 deposition.[86] As protons are locally consumed, the interfacial pH shifts dynamically, creating microenvironments that

favor side reactions such as Mn^{3+} disproportionation.[75] These evolving local conditions promote preferential nucleation at sites with elevated Mn^{2+} concentrations, structural defects, or favorable pH, reinforcing pre-existing heterogeneity. The result is spatially uneven redeposition of MnO_2 and non-uniform phase formation, with variations in lattice structure, crystallographic orientation, and local electrochemical activity.

Reaction-induced heterogeneity in thick MnO_2 cathodes also accelerates structural degradation. Unlike intercalation-only systems, which undergo relatively modest lattice breathing, cyclic dissolution of Mn to Mn^{2+} followed by redeposition as MnO_2 imposes large, localized volume swings throughout the porous matrix. Because the dominant reaction pathway varies spatially, these volumetric changes are inherently non-uniform, concentrating strain in specific domains. The resulting mechanical stresses scale with areal capacity and are especially severe in thick electrodes, where absolute expansion and contraction per cycle are larger. Compounding this, freshly electrodeposited MnO_2 is often mechanically brittle, so strain localizes at grain boundaries and interparticle necks, seeding cracks that propagate with cycling.[87] Crack growth disrupts ionic pathways and the electronic percolation network. Once fractures coalesce, interfacial delamination from the current collector becomes likely, which increases local contact resistance and creates current hot spots that further bias reaction heterogeneity. These coupled processes sever electronic and ionic pathways, isolating portions of the active material into "dead" zones that no longer participate in redox reactions.[75] As current is forced through the remaining conductive channels, local overpotentials and mechanical stress intensify, accelerating both chemical degradation and structural failure. The net result is a self-reinforcing cycle of capacity fading and mechanical disintegration that worsens with increasing cycle number, operating rate, and electrode thickness.

2.2.3. Manufacturing limitations. Apart from the electrochemical challenges discussed above, the fabrication of thick MnO_2 electrodes faces intrinsic manufacturing limitations. Conventional slurry-casting methods, such as tape casting or slot-die coating, encounter two primary processing bottlenecks during drying.

The first limitation is vertical stratification, in which an uneven particle distribution develops through the electrode thickness. This phenomenon arises from the competition between particle diffusion, which promotes uniformity, and evaporation-driven convection, which carries particles toward the drying interface. Their relative effects are captured by the Péclet number:[88]

$$Pe = \frac{H\dot{E}}{D}$$

where H is the film thickness, $\dot{E}$ the solvent evaporation rate, and D the particle diffusion coefficient. When $Pe < 1$, diffusion dominates and the film remains homogeneous; when $Pe > 1$, rapid evaporation causes particle migration and surface "skinning".[89] In thick MnO_2 electrodes, the large H raises Pe above unity for all components, while differences in particle size and

density further drive segregation. As a result, heavier MnO_2 microparticles settle toward the bottom, whereas smaller conductive carbon and binder migrate upward. This compositional gradient leads to surface regions enriched in conductive additives but deficient in active material, while deeper layers suffer from poor electronic connectivity, reducing overall utilization during cycling.

The second issue, crack formation, originates from capillary stresses at the air–solvent interface during drying. As film thickness increases, capillary pressure and the associated tensile stress rise sharply and can exceed the film's mechanical strength.[85,90] Above the critical cracking thickness (CCT), the electrode develops cracks and delaminates from the current collector, degrading mechanical integrity and adhesion. Nanoparticulate films are more susceptible to capillary stresses and therefore often exhibit a much lower CCT than films made with microparticles. Consequently, although nano-MnO_2 can provide faster ion transport and better rate performance, the thickness required for high areal capacity frequently exceeds the CCT, making conventional slurry casting unsuitable for high-loading fabrication.

To overcome these challenges, several alternative processing strategies have been proposed. For example, semi-dry or dry processing mechanically mixes MnO_2, conductive carbon, and binder powders with minimal or no solvent to form a viscous paste that is directly pressed or coated onto the current collector. By avoiding solvent evaporation, this approach eliminates stratification and capillary-stress-driven cracking. Recent reports demonstrate MnO_2 mass loadings up to 80 mg cm^{-2} using semi-dry processing.[91] However, achieving homogeneous particle dispersion without solvent remains difficult. Conductive carbon and binder particles (e.g., polytetrafluoroethylene) tend to aggregate, creating locally resistive or mechanically weak regions with higher susceptibility to cracking or delamination during calendering or cycling.

As an alternative, three-dimensional (3D) printing enables precise, layer-by-layer assembly of architected electrodes. This technique allows deliberate control over porosity, tortuosity, and surface area to optimize both mechanical properties and electrochemical performance by improving electrolyte penetration depth and reducing concentration gradients.[92] For example, Yao et al. prepared a printable ink by dispersing α-MnO_2, conductive carbons, and binders in solvent.[93] Using this ink, they fabricated thick electrodes with a MnO_2 mass loading of ~15 mg cm^{-2}, which delivered an initial areal capacity of 1.7 mAh cm^{-2} at high current of 1 A g^{-1}.

Another strategy involves the electrolytic Zn–MnO_2 cell configuration, in which MnO_2 is first electrodeposited onto a current collector before transitioning to conventional battery operation. With Mn^{2+} pre-loaded in the electrolyte, the cell is initially charged to deposit a conformal MnO_2 layer of tunable thickness, enabling precise control over cathode loading. Two issues warrant attention. First, the crystallinity of the deposited MnO_2 is highly sensitive to deposition parameters such as temperature and electrolyte chemistry. For example, Cui et al. reported that an increase in temperature (from 25 to 75 °C)

drives a phase transition from ε-MnO_2 to γ-MnO_2, the latter exhibiting superior reaction kinetics.[30] More recently, the same group introduced a soft-template electrolyte additive that promotes the ε- to δ-MnO_2 transition during electrodeposition.[94] Second, the efficiency of electrodeposition depends strongly on the substrate. Deposition on conventional substrates such as carbon fiber or carbon cloth often results in crack formation, mechanical delamination, and Mn loss, particularly at high areal capacities.[87,95]

Overall, overcoming the thick-electrode barrier to realize high-areal-capacity Zn–MnO_2 batteries requires the synergistic design of both MnO_2 active materials and electrode architectures. Beyond the prevailing focus on tailoring MnO_2 chemistry and morphology, increasing attention has shifted toward mitigating reaction-kinetic limitations and spatial heterogeneity that emerge in thick electrodes, as well as addressing manufacturability challenges. Nevertheless, the thick-electrode barrier is currently defined primarily in terms of mass loading or areal capacity, while quantitative descriptors, such as porosity, tortuosity, effective ionic penetration depth, and internal stress during electrodeposition, remain largely unexplored for thick MnO_2 electrodes.

3. Recent advances in high-loading Zn–MnO_2 batteries

3.1. Lattice modification

As discussed in section 2, pristine MnO_2 inherently suffers from sluggish reaction kinetics due to its intrinsically low electronic conductivity. In addition, the presence of Mn^{3+} within the lattice can induce structural deformation of the [MnO_6] octahedra, known as Jahn–Teller distortion, which leads to irreversible phase transitions and further degrades structural stability. Both challenges, rooted in the lattice characteristics of MnO_2, significantly limit its electrochemical performance, especially under high mass loading conditions.[96] Consequently, rational lattice design of MnO_2 is critical for improving its electrochemical reaction kinetics and redox reversibility.[97–100]

Heteroatom doping has emerged as an effective strategy for tailoring the lattice structure and electrochemical properties of MnO_2. Over the past decades, a wide range of dopants have been explored, including anions such as S[101,102] and N[102,103] as well as cations such as Ce^{3+}/Ce^{4+},[104] Ni^{2+},[105] Mo^{4+},[106] Mg^{2+},[107] Fe^{3+},[108] and Co^{2+}.[108] For substitutional doping, anions typically replace O-sites, thereby tuning the electronegativity and local coordination environment,[54,109] whereas cations substitute Mn-sites and incorporate foreign metal ions into the MnO_2 framework, providing complementary effects such as lattice stabilization and electronic structure modulation.[47,108,110,111] In addition, interlayer doping can expand the interlayer spacing or tunnel size, enhancing Zn^{2+}/ H^+ intercalation/deintercalation kinetics and thereby improving the rate performance.[112]

However, it is worth noting that most doping strategies have yet to be validated under industrially relevant conditions

such as high mass loading electrodes or in pouch cell configurations, leaving uncertainties about their practical impact. Recently, as more concern from the practicality perspective, advanced heteroatom doping designs have been demonstrated in high-loading Zn–MnO$_2$ batteries. For example, Ji *et al.* introduced Se into δ-MnO$_2$, yielding Se–MnO$_2$ where Se atoms replace lattice oxygen to form stable Mn–Se bonds (Fig. 3a).[97] This substitution modulates the local electronic environment, reducing the Mn–O octahedral distortion and lowering the Jahn–Teller-driven Mn dissolution. Importantly, Se doping regulates H$^+$ intercalation while facilitating Zn^{2+} diffusion (Fig. 3b and c), thereby minimizing electrolyte pH fluctuations

and inhibiting the formation of inactive ZnMn$_2$O$_4$ byproducts. As a result, pouch cell tests under moderate loading (4 mg cm^{-2}) demonstrate stable cycling (213 mAh g^{-1} at 1 A g^{-1} for 65 cycles).

The effect of dual-ion doping has also gained increasing attention, as it is considered more efficient due to potential synergistic effects. For instance, Liu *et al.* incorporated N and S dopants into the δ-MnO$_2$ lattice *via* calcination, yielding NS-MnO$_2$ with enhanced electronic conductivity and structural stability.[102] As a result, the electrode exhibited a high reversible specific capacity of 295 mAh g^{-1} at 0.2 A g^{-1} over 110 cycles. He *et al.* reported a Cu^{2+} and Na$^+$ co-intercalated
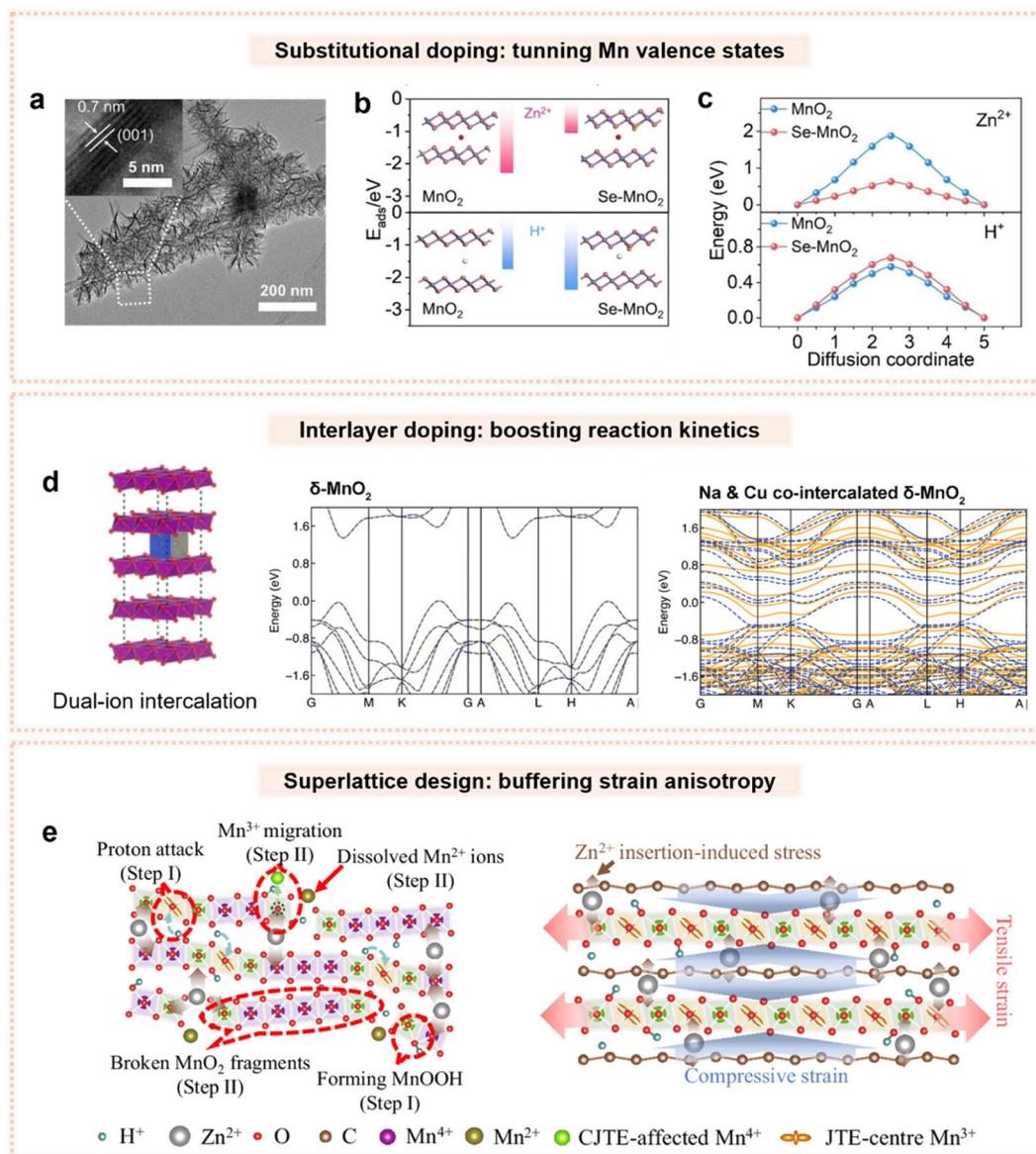

Fig. 3 (a) Transmission electron microscopy (TEM) image of Se-MnO$_2$ with insets showing resolved lattice. (b) Adsorption energies of Zn^{2+} and H$^+$ on MnO$_2$ and Se-MnO$_2$. (c) Diffusion energy barrier of Zn^{2+} and H$^+$ migration in MnO$_2$ and Se-MnO$_2$.[97] (d) Schematic of dual-ion intercalation of δ-MnO$_2$ and the corresponding impact on band structures based on DFT modelling.[113] (e) Schematic illustration showing the CJTE in improving structural stability of MnO$_2$/graphene superlattice electrodes.[120]

δ-MnO$_2$ (NCMO), where the simultaneous introduction of Cu and Na increases the number of electronic bands crossing the Fermi level, effectively creating additional charge conduction pathways (Fig. 3d).[113] This dual doping strategy amplifies the catalytic activation of Mn^{4+}/Mn^{2+} redox couples by Cu^{2+}, resulting in improved capacity and cycling stability. As a result, the high-loading NCMO cathode (10.9 mg cm^{-2}) delivered a reversible areal capacity of 2.10 mAh cm^{-2} after 50 stable cycles.

Defect engineering provides an alternative route to tune the MnO$_2$ lattice structure by introducing defects (*e.g.*, oxygen vacancies) that create localized states facilitating electron hopping and enhancing Zn^{2+} adsorption.[70,99,100,114] Notably, defect engineering is often employed alongside heteroatom doping to achieve synergistic effects. Techniques, such as thermal annealing,[115] plasma treatment,[116] or reductive doping,[108] produce defect-rich MnO$_2$ with enhanced conductivity and catalytic activity. For example, Wu *et al.* synthesized δ-MnO$_2$ with a synergistic combination of oxygen vacancies and K$^+$ pre-intercalation starting from low-cost γ-MnO$_2$, effectively improving Zn^{2+} intercalation kinetics.[117] Sun *et al.* introduced more oxygen vacancies by compositing MnO$_2$ with MoO$_3$, which weakened Mn–O bonds and enhanced electron transport.[70] The resulting material achieved a high specific capacity of 333 mAh g^{-1} and exhibited stable cycling performance in Mn^{2+}-free electrolytes.

Beyond heteroatom doping and defect engineering, constructing superlattice structures by integrating other functional materials into the MnO$_2$ lattice has emerged as another promising strategy. Superlattices can introduce additional charge transfer pathways, enhance electronic delocalization, and enable tunable interlayer interactions that together improve reaction kinetics and structural stability under deep cycling.[118] For example, Bai *et al.* reported a quinone-functionalized MnO$_2$ superlattice that enables tunable interlayer d–π interactions through organic–inorganic p–π–d conjugation.[119] This electronic modulation enhances Mn t$_2$g orbitals orbital occupancy, stabilizes the [MnO$_6$] octahedra against lattice distortion during deep Zn^{2+} intercalation, and accelerates Zn^{2+}/H$^+$ co-insertion. Wang *et al.* proposed leveraging the cooperative Jahn–Teller effect (CJTE) to mitigate charge disproportionation by constructing a superlattice structure through electrostatic self-assembly of monolayer-stacked δ-MnO$_2$ and positive-charged graphene nanosheets.[118] In this design, the CJTE not only distorts individual [Mn(III)O$_6$] octahedra but also propagates orbital ordering to neighboring [Mn(IV)O$_6$] octahedra through shared edges, thereby inducing in-plane tensile and out-of-plane compressive strains (Fig. 3e).[120] Within the superlattice, the strong charge transfer between MnO$_2$ and graphene enhances electronic conductivity and enables superior rate performance, while the long-range biaxial strain reinforces lattice stability under deep cycling.

3.2. Surface coating

While lattice structure tailoring can improve redox reaction kinetics and bulk phase reversibility, it is usually insufficient to fully suppress interfacial side reactions or ensure chemical robustness. In this context, MnO$_2$ surface coating and protective strategies have emerged as alternative tools to complement MnO$_2$ modifications and stabilize the cathode–electrolyte interface.[121]

One widely explored method involves inorganic surface coatings that act as physical barriers while simultaneously tuning the local electronic environment. For instance, Lin *et al.* introduced TiO$_2$ nanolayers with oxygen vacancies, forming Ti–O–Mn bonds at the interface and creating an electron-rich region that enhanced charge transfer and reduced interfacial valence fluctuations.[122] The TiO$_2$ layer also acted as a chemically stable and conformal barrier that mitigated Mn^{2+} dissolution, buffered volume changes, and reduced parasitic reactions with the electrolyte. As shown in Fig. 4a, the calculated dissolution energy of a single Mn atom in MnO$_2$@TiO$_2$ (3.25 eV) was significantly higher than that of bare MnO$_2$ (2.06 eV), indicating stronger lattice cohesion and greater resistance to structural degradation during cycling. This stabilizing effect was further supported by inductively coupled plasma-optical emission spectrometer (ICP-OES) analysis. After 200 cycles, the Mn concentration in the electrolyte dropped to 6.45 mg L^{-1} for MnO$_2$@TiO$_2$—only one-sixth of that measured for the uncoated MnO$_2$ electrode (Fig. 4b).

Beyond suppressing Mn dissolution, certain coatings can serve as a cathode–electrolyte interface (CEI), stabilizing the electrode by buffering local pH fluctuations. Zhou *et al.* reported an electro-chemo-structural interface of zinc phosphate (Zn$_3$(PO$_4$)$_2$) and ammonium (NH$_4^+$) on the MnO$_2$ cathode, termed PN–MnO$_2$ (Fig. 4c).[123] The PO$_4^{3-}$/NH$_4^+$ pair effectively buffers local pH changes (Fig. 4d), while Zn$_3$(PO$_4$)$_2$ enabled a reduced activation energy for ionic diffusion, facilitating ion transport and improving capacity utilization. Consequently, PN–MnO$_2$ maintains stable Mn content with minimal byproduct accumulation, delivering 12 mAh cm^{-2} over 80 cycles in pouch cells at 5 mA cm^{-2}.

Increasing attention has also been devoted to organic coatings as alternative interfacial regulators. For instance, isoleucine forms Mn–N interfacial bonds that reinforce the α-MnO$_2$ surface and inhibit Mn dissolution. The resulting isoleucine-α-MnO$_2$ structure enables 3D Zn^{2+} diffusion and benefits from oxygen vacancies, collectively enhancing conductivity, ion transport, and cycling reversibility.[65] Organophosphonic acids like aminopropyl phosphonic acid (AEPA) could create a hydrophobic coating that physically isolates the electrode from the electrolyte (Fig. 4e and f).[124] This significantly inhibits Mn^{2+} leaching and improves redox reversibility. Beyond synthetic molecules, naturally derived polyphenols such as tannic acid offer a sustainable and effective means of interfacial regulation.[125] Rich in hydroxyl groups, tannic acid chelates dissolved Mn^{2+} and stabilizes the local interfacial environment without interfering with Zn^{2+} intercalation.

Finally, some organic coatings function as selective ion-transport layers, simultaneously stabilizing the interface and improving reaction selectivity. Sun *et al.* designed a polyaniline (PANI) nanolayer coating on MnO$_2$ cathode to enhance interfacial ion transport and stability (Fig. 4g).[126] The conductive
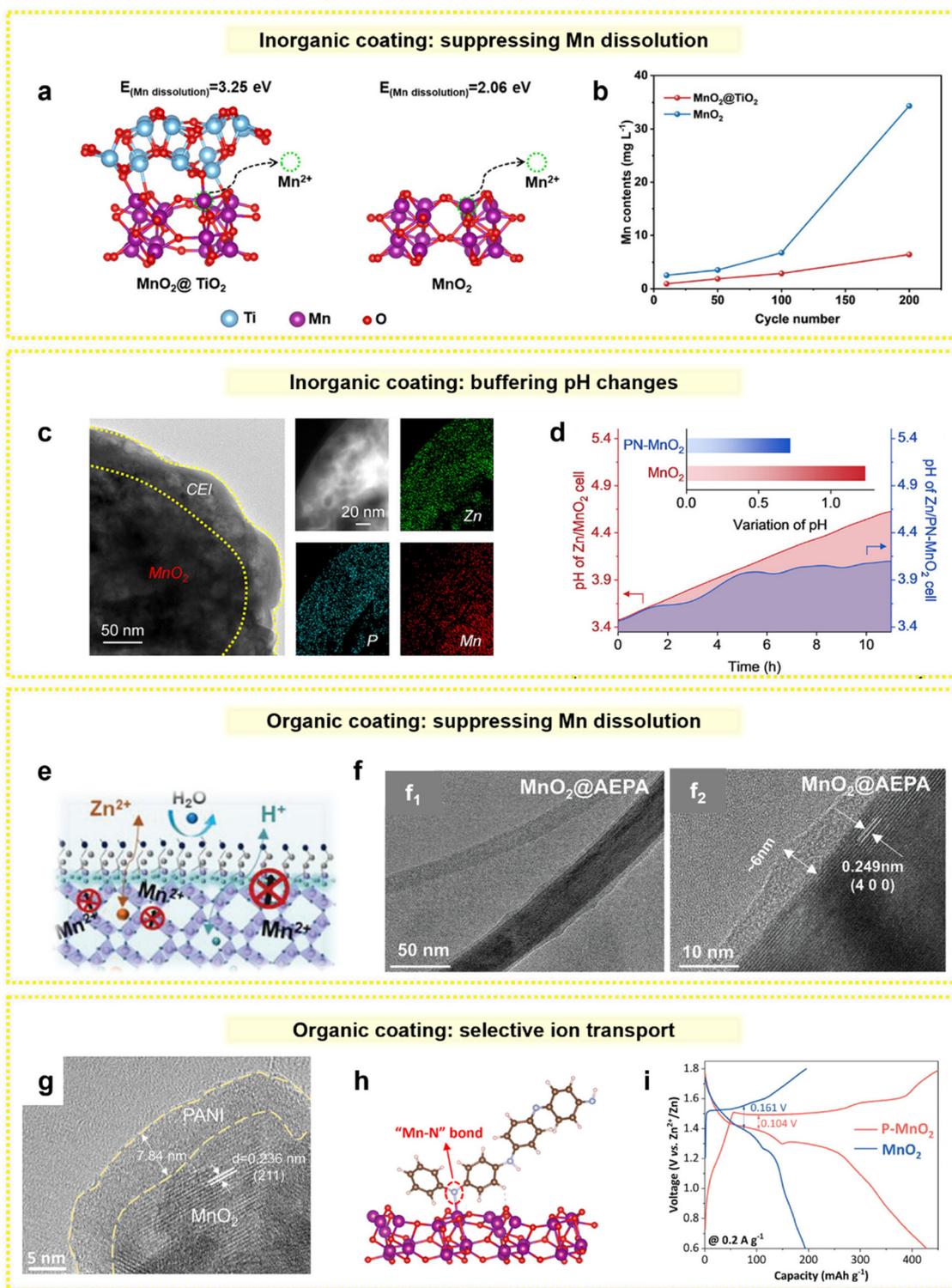
Fig. 4 (a) Calculated Mn dissolution energy for $MnO_2@TiO_2$ and pristine MnO_2. (b) Mn content in the electrolyte (without Mn salt added) after different cycles at 0.5 A g^{-1}.[122] (c) TEM image with EDS elemental mapping of PN−MnO_2. (d) In situ pH variation in electrolyte close to PN−MnO_2 and bare MnO_2.[123] (e) Schematic illustration of the interfacial protection mechanism enabled by the AEPA electrolyte additive. (f) TEM (f_1) and high resolution TEM (HRTEM) (f_2) images of MnO_2 after AEPA surface modification.[124] (g) HRTEM image of PANI-coated MnO_2. (h) Proposed structural model of PANI-coated MnO_2 featuring Mn−N interfacial bonding. (i) Galvanostatic charge/discharge profiles of PANI-coated MnO_2 at 0.2 A g^{-1}.[126]

PANI layer facilitates proton conduction and acts as a selective barrier, regulating Zn^{2+} intercalation and promoting MnO_2 redeposition through the formation of Mn–N interfacial bonds and a proton-rich environment (Fig. 4h). These interfacial improvements significantly lower polarization voltage and enhance redox kinetics (Fig. 4i). As a result, the PANI-coated MnO_2 cathode with a mass loading of 23.5 mg cm^{-2} demonstrated exceptional durability, delivering 171 mAh g^{-1} at 0.03 A g^{-1} over 110 cycles. A maximum capacity of 1.5 Ah at 0.15 mA cm^{-2} with 99.1% coulombic efficiency after 11 cycles was reported in series-connected pouch cells based on PANI-coated MnO_2.

3.3. Substrates design

As discussed above, achieving uniform ion and electron distribution across the electrode is critical for high-performance MnO_2 cathodes, as it promotes efficient ion transport, mitigates local current density hotspots, and regulates reaction kinetics.[108,127] However, in conventional planar electrodes, current density often concentrates near the surface, leading to uneven utilization of active material at the top layer. To overcome this limitation, 3D current collectors are widely employed for high-loading MnO_2 electrodes.[128] Their interconnected conductive networks and large surface area redistribute electron and ion flux, enabling uniform electrochemical reactions and improved cycling stability.[129] Although the introduction of a 3D architecture inevitably increases the volume and mass of the battery, thereby reducing energy density, the resulting higher electrochemical efficiency makes such designs better suited for applications in which energy density is not the primary constraint, such as grid-scale LDES and other stationary storage systems.

Carbon-based substrates are widely used for this purpose due to their flexibility, mechanical strength, moderate porosity, and good electrical conductivity. In addition, their lightweight nature, cost-effectiveness, and chemical stability in acidic electrolytes make them more attractive than metallic substrates. Typically, MnO_2 is integrated onto carbon scaffolds such as carbon cloth,[130–132] carbon felt,[7,133] and carbon paper,[134,135] which serve as cathodes in AZIB research or as deposition substrates in electrolytic Zn–MnO_2 batteries, where the cell is first charged to electrodeposit MnO_2 to achieve high areal loadings.

As uniform electrodeposition is critical for achieving highly reversible MnO_2 utilization, the growing interest in high areal-capacity Zn–MnO_2 batteries has intensified efforts to understand how the morphology and surface chemistry of current collectors govern deposition behavior. For example, Majumder et al. systematically studied MnO_2 electrochemistry on various carbon substrates, including carbon cloth, graphite felt, and carbon nanotube (CNT) frameworks.[136] Their findings revealed that defect-rich surfaces with abundant oxygen-containing functional groups in carbon cloth and graphite felt promote better ionic transport and faster deposition–dissolution compared to CNTs.

Additionally, Li et al. demonstrated that at high deposition capacities, MnO_2 becomes increasingly susceptible to nonuniform deposition, which promotes stress accumulation and ultimately leads to crack formation in dense MnO_2 layers. Such deposition-heterogeneity-induced material detachment was identified as a primary cause of capacity fading and poor cycling stability (Fig. 5a).[87] Specifically, large cracks appeared after depositing 10 mAh cm^{-2} of MnO_2 on pristine carbon fiber (PCF), which subsequently led to bulk MnO_2 detachment during discharge (Fig. 5b). To address this, they introduced CNT frameworks onto carbon felt (CNT/CF) *via in situ* vapor-phase growth, guiding the uniform deposition of porous MnO_2 and thus alleviating mechanical stress. As a result, the electrode exhibited crack-free MnO_2 deposition even after plating 40 mAh cm^{-2} (Fig. 5c), and the full cell achieved stable cycling over 200 cycles at a high areal capacity of 15 mAh cm^{-2}.

To further improve MnO_2 utilization in carbon scaffolds, researchers have developed surface modifications and interfacial chemical strategies to enhance redox kinetics and structural stability at the molecular level. For instance, Li et al. proposed a two-step electrodeposition approach to construct an organic–inorganic hybrid structure, in which MnO_2 deposits are partially embedded within poly(4,4′-oxybisbenzenamine) (PODA) nanosheets onto nanoporous carbon (Fig. 5d).[137] The resulting C@PODA/MnO_2 architecture establishes strong Mn–N bonds that both enhance Zn^{2+} adsorption and suppress Mn dissolution (Fig. 5e), while the PODA provides additional active sites (C=N) for Zn^{2+} storage. At higher-loading configuration (6.8 mg cm^{-2}), the electrode delivered an areal capacity of 1.7 mAh cm^{-2} (250 mAh g^{-1} at 0.1 A g^{-1}) and maintained good rate capability (56 mAh g^{-1} at 5.0 A g^{-1}).

Other functional coatings and surface modifiers have also been explored to guide MnO_2 electrodeposition. Lan et al. introduced a manganese-based Prussian blue analog (Mn-PBA) seed layer on graphite foil, providing anchoring sites for uniform MnO_2 growth.[138] Fan et al. decorated carbon paper with Bi-MOF, which effectively directed Mn^{2+} deposition while gradually releasing Bi^{3+} to reinforce the structural stability of the deposits.[139] Similarly, Zhu et al. electrodeposited Bi/rGO composites onto carbon paper, as a substrate for the *in situ* growth of MnO_2 nanoflakes.[134] Li et al. used electrodeposited NiMn-layered double hydroxide nanosheets on carbon cloth to induce local charge accumulation and form strong Mn–O bonds, thereby promoting favorable MnO_2 deposition.[140] However, despite these advances, most studies have yet to demonstrate the effectiveness of these strategies under high-loading MnO_2 configurations.

To further optimize the geometry of 3D electrode architectures, techniques such as 3D printing and templating have been widely adopted to construct frameworks with precisely controlled porosity and tortuosity. Beyond the previously mentioned work on 3D printing MnO_2-containing inks, 3D printing has also been explored for fabricating advanced current collector substrates. For instance, Wu et al. employed direct-ink 3D printing followed by high-temperature annealing to produce graphene/CNT-based carbon microlattices (3DP CMs) with tunable periodicity and tailored surface functionality.[95] The
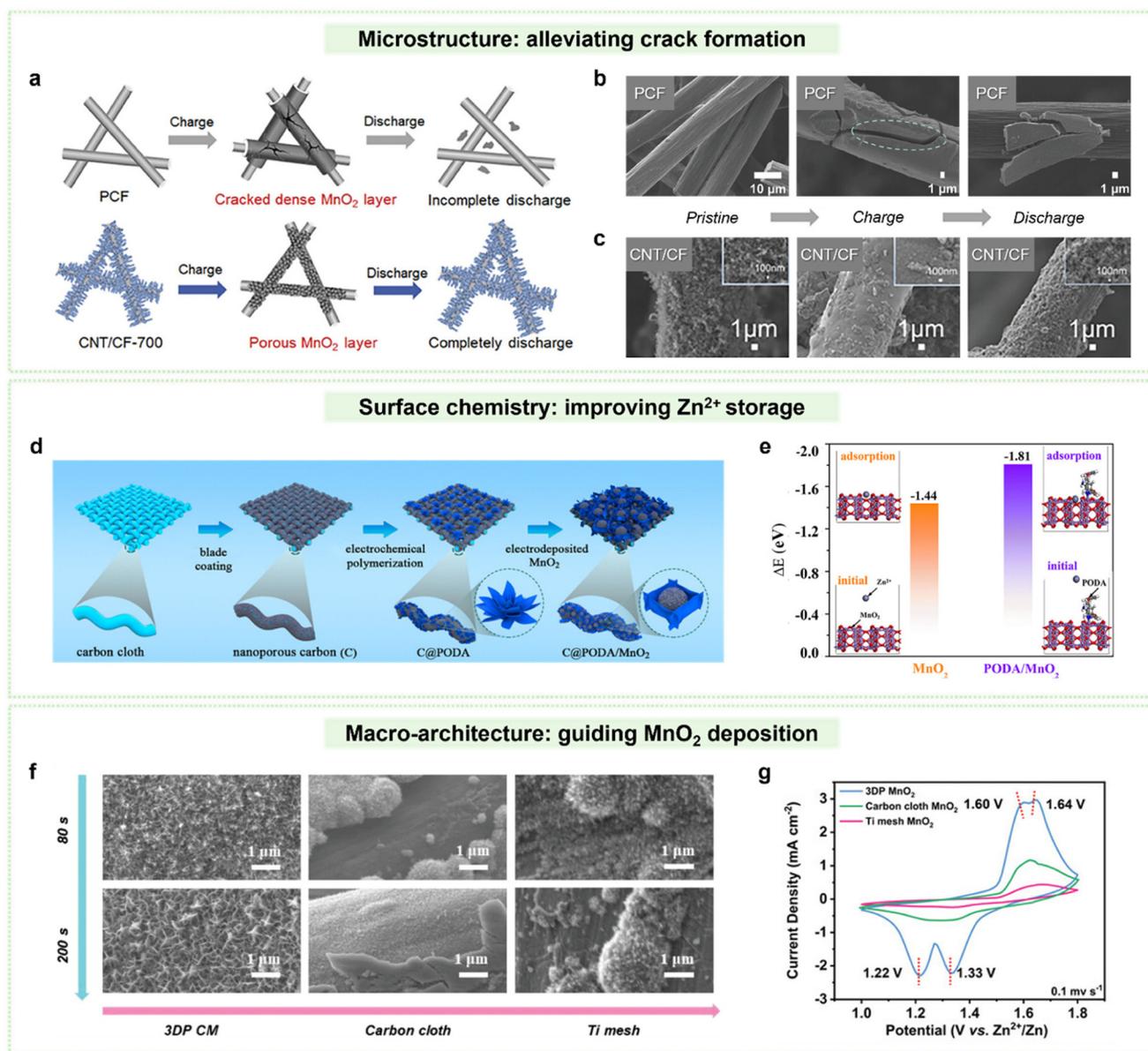
Fig. 5 (a) Schematic illustration of the distinct MnO_2 deposition/dissolution behavior on PCF and CNT/CF electrodes. (b and c) Comparison of morphological evolution of PCF (b) and CNT/CF composite electrodes (c) during charging/discharging.[87] (d) Schematic of the two-step fabrication process forming the organic−inorganic hybrid C@PODA/MnO_2. (e) Calculated Zn^{2+} adsorption energies of MnO_2 and PODA/MnO_2.[137] (f) Surface morphology evolution of 3DP CM, carbon cloth, and Ti mesh during MnO_2 electrodeposition. (g) CV curves of AZIBs using MnO_2-deposited 3DP CM, MnO_2-deposited carbon cloth, and MnO_2-deposited Ti mesh electrodes at a scan rate of 0.1 mV s^{-1}.[95]

ordered macroporous lattice created a more uniform local electric field, while defect-rich carbon surfaces formed during annealing promoted Mn^{2+} adsorption and accelerated nucleation. Conformal and dense MnO_2 growth was achieved on the 3DP CM substrate, whereas conventional carbon cloth and Ti mesh exhibited sparse and non-uniform deposition (Fig. 5f). Cyclic voltammetry (CV) measurements of MnO_2-deposited 3DP CM (3DP MnO_2) further revealed two pairs of redox peaks, corresponding to a two-step H$^+$ and Zn^{2+} co-insertion/extraction process (Fig. 5g). The larger enclosed area of the CV curves also indicates higher utilization of active material. As a

result, the high-loading cathode (28.4 mg cm^{-2}) achieved an areal capacity of 8.04 mAh cm^{-2}, corresponding to a gravimetric capacity of 282.8 mAh g^{-1}, and retained 80.2% capacity retention after 500 cycles at 10 mA cm^{-2}.

Extensive efforts have also focused on coupling lattice doping with advanced structural designs to simultaneously address transport limitations and enhance active material utilization in thick MnO_2 electrodes. For example, Amine *et al.* combined K$^+$ doping with a vertically aligned MnO_2 nanowire architecture, stands out for successfully integrating K$^+$ doping with a vertically aligned nanowire architecture, simultaneously

achieving high mass loading (20.2 mg cm^{-2}) and notable energy density (77 Wh kg^{-1} sustained over 350 cycles).[141] Ye *et al.* designed a K-δ-MnO$_2$/Ti$_3$C$_2$T$_x$ MXene cathode paired with K$_2$SO$_4$ electrolyte additive, where the Ti$_3$C$_2$ skeleton and K$^+$ ions synergistically stabilize the MnO$_2$ structure, suppress Mn dissolution, and provide extra active sites for Mn^{2+} deposition, achieving a high capacity of 502.2 mAh g^{-1} at 0.3 A g^{-1}.[142]

3.4. Electrolyte optimization

Beyond engineering the components of the MnO$_2$ electrode itself, electrolyte design is widely regarded as one of the most effective approaches to further enhance the performance of

Zn–MnO$_2$ batteries.[143,144] In 2016, Liu *et al.* pioneered the addition of MnSO$_4$ to the conventional ZnSO$_4$ electrolyte to suppress Mn dissolution—a strategy that has since been widely adopted in subsequent studies till today, demonstrating the effectiveness of electrolyte additives.[9] More recently, as deeper insights have been gained into the reaction mechanisms and failure modes of MnO$_2$ cathodes in acidic electrolytes, the rational design of electrolyte systems has advanced accordingly.

Electrolyte engineering plays a crucial role in enhancing the rate performance of thick electrodes, particularly given the intrinsically sluggish reaction kinetics of MnO$_2$. Chen *et al.*
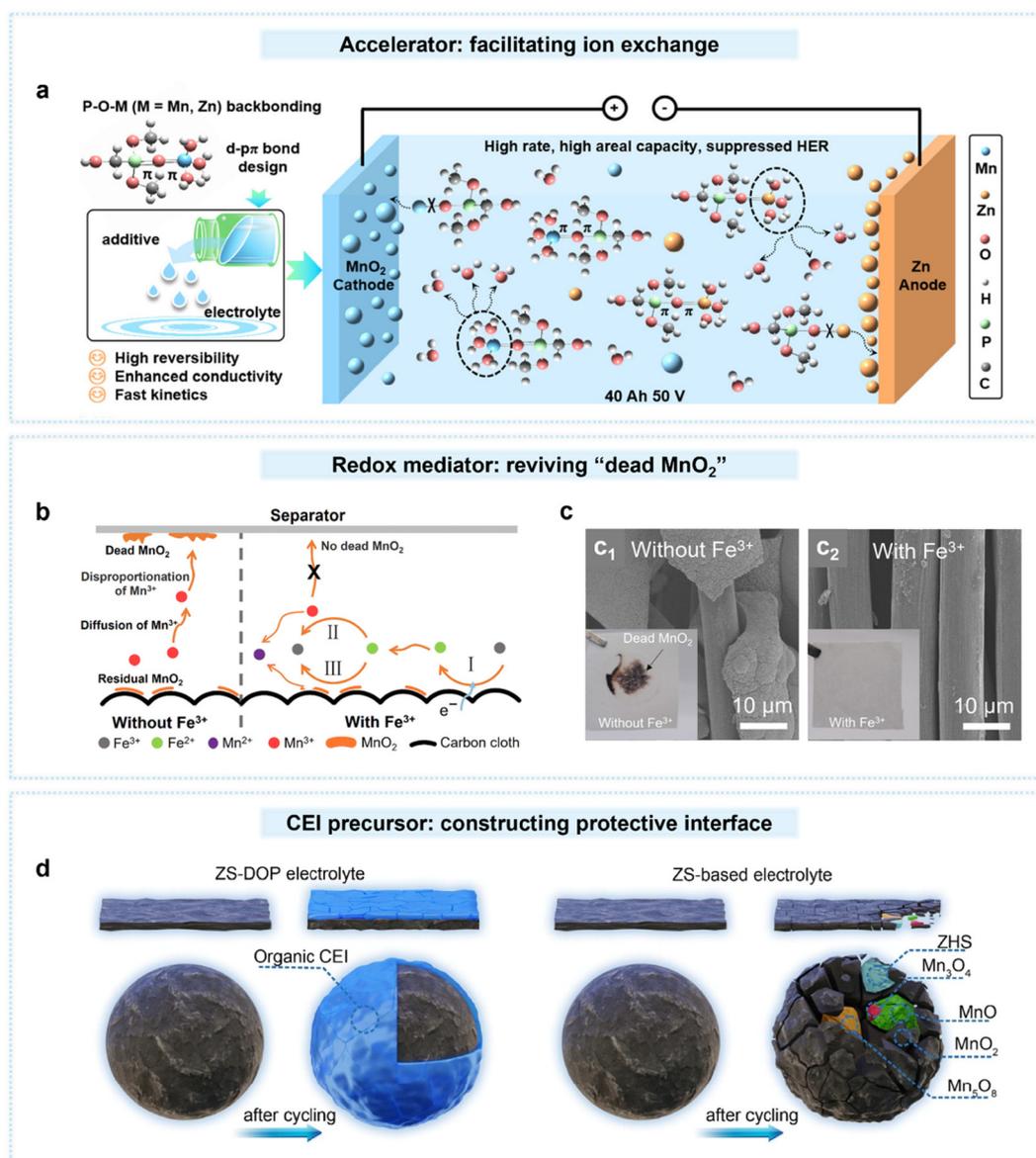

Fig. 6 (a) Design and working mechanism of P–O–M d–pπ backbonding in electrolytic Zn–MnO$_2$ batteries.[146] (b) Schematic illustration of "dead" MnO$_2$ formation and the working mechanism of the redox mediator Fe^{3+}/Fe^{2+} couple. (c) Surface morphologies of carbon cloth and optical photographs of separators after cycling in electrolytes (c$_1$) without and (c$_2$) with Fe^{3+}/Fe^{2+} redox pair in Cu–MnO$_2$ system.[75] (d) Schematic illustration of an *in situ* formed CEI derived from DOP additives, acting as a hydrophobic protective layer to mitigate Mn dissolution.[91]

introduced the concept of a cationic accelerator (CA) to promote the solvation/desolvation processes, thereby improving the kinetics of both the cathodic MnO_2/Mn^{2+} and anodic Zn/Zn^{2+} reactions.[145] The resulting $Zn–MnO_2$ battery incorporating the CA demonstrated impressive rate capability, achieving large reversible capacities of 455 mAh g^{-1} and 3.64 mAh cm^{-2} at 20 C, alongside long-term cycling stability exceeding 2000 cycles. More recently, Chai et al. designed an auxiliary molecule to construct P–O–M (M = Mn, Zn) d–pπ backbonding, which not only facilitates rapid cation capture during charging, promoting deposition, but also aids quick cation release during discharging, supporting efficient dissolution (Fig. 6a).[146] As a result, the $Zn–MnO_2$ full cell demonstrate a capacity retention of 94% after 1500 cycles at a high areal capacity of 14.05 mAh cm^{-2}. To further demonstrate its practical use, a scaled-up soft-pack battery delivered over 1.60 Ah at a discharge rate of 0.5 C and retained a coulombic efficiency of

~80% over 100 cycles. Impressively, an assembled 40 Ah battery successfully powered an electric vehicle over a demonstration distance of 10 km.

Another important challenge is the complex set of reactions during the discharge process of MnO_2 and the need for controlled reaction selectivity to pursue higher specific capacity. Zhi et al. proposed using an amphiphilic hydrogel electrolyte with a wide electrochemical stability window and adequate Zn^{2+} ion channels, which creates a voltage plateau discrepancy between Zn^{2+} and H^+ intercalation.[32] This design enables the system to distinguish MnO_2/Mn^{2+} conversion, Zn^{2+} intercalation, and H^+ conversion occurring at different potentials. Similarly, Sun et al. used $Zn(H_2PO_4)_2$ as a proton reservoir; during discharge, $Zn(H_2PO_4)_2$ deprotonates to $Zn_3(PO_4)_2$, and the released protons facilitate the reduction of MnO_2 to Mn^{2+} while maintaining a high redox voltage of 1.75 V.[147] Cheng et al. demonstrated that a simple $Zn(ClO_4)_2$ aqueous electro-
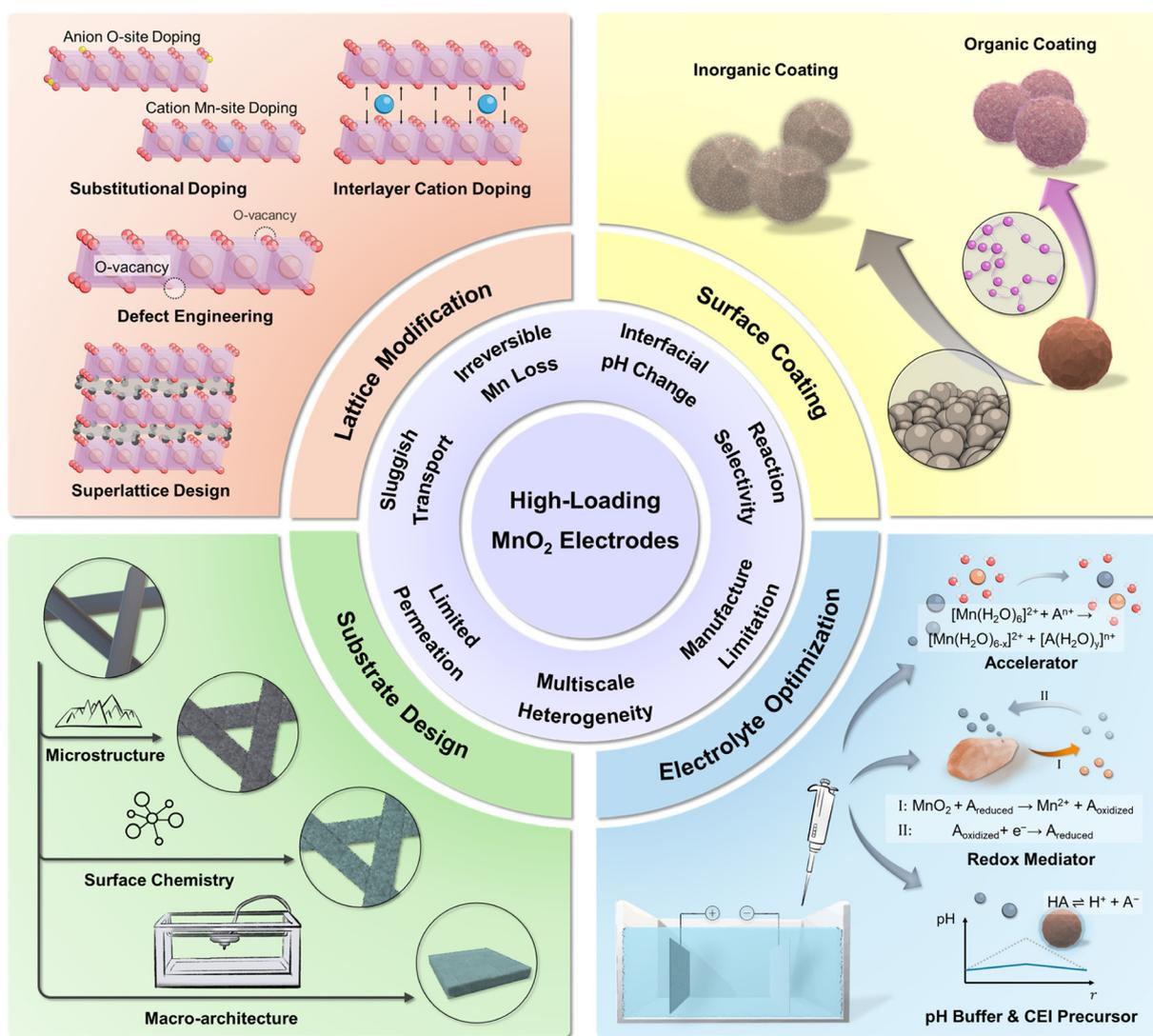

Fig. 7 Summary of the challenges associated with high-loading MnO_2 electrodes and the rational design strategies for high-performance Zn–MnO_2 batteries.

lyte, with its high ionic conductivity even when frozen, could shift the dominant reaction from problematic H^+ insertion at room temperature to primarily Zn^{2+} insertion at subfreezing temperatures.[148] This system achieved high-energy-density prototypes with a practical N/P ratio of 1.5 (8 mAh cm^{-2} MnO_2) and a low E/C ratio of 2 g Ah^{-1}.

Electrolyte engineering also plays a critical role in mitigating Mn loss caused by "dead MnO_2" formation, with certain additives acting as redox mediators. These mediators introduce an additional redox couple that actively participates in the MnO_2/Mn^{2+} redox cycle, enabling the reversible reactivation of inactive Mn species during cycling. Specifically, Mn^{3+} species (such as Zn_xMnO_2 and MnOOH), typically formed through intercalation or hydrolysis, and Mn^{4+} species remaining as residual MnO_2 from detachment or Mn^{3+} disproportionation, can be chemically reduced back to soluble Mn^{2+} by the mediator. This process redissolves inactive Mn compounds and suppresses cumulative Mn loss (Fig. 6b). As a proof of concept, Yang et al. demonstrated in a Cu–MnO_2 system that adding 10 mM Fe^{3+}/Fe^{2+} redox couple effectively reactivated these inactive species, thereby mitigating Mn dissolution (Fig. 6c).[75] The study also showed that other mediators, such as Br_2 and organic species like 2,2,6,6-tetramethyl-piperidinyloxyl (TEMPO), can similarly restore lost active material and stabilize cycling.

Recently, Zhou et al. introduced $Al_2(SO_4)_3$ and hydroquinone (HQ) as additives (Al-HQ), where HQ serves as the redox mediator and Al^{3+} co-deposits or intercalates into MnO_2, modulating its electronic structure.[149] The resulting Zn/Al-HQ/MnO_2 battery with a high areal capacity of 10.7 mAh cm^{-2} delivered 99% of its initial capacity after 100 cycles (E/C ~0.1 mL mAh^{-1}). Additionally, Li et al. demonstrated a vanadyl/pervanadyl (VO^{2+}/VO_2^+) redox-mediated interface.[150] With MnO_2 loadings ranging from 50 to 155 mg cm^{-2}, the electrodes achieved nearly linear increases in areal capacity, reaching an average specific capacity of 593 mAh g^{-1} and delivering an areal capacity up to 100 mAh cm^{-2} (E/C ~0.6 mL mAh^{-1}), with an estimated cost of $3.17 per kWh.

Finally, another significant advance in electrolyte design is its ability to effectively regulate the local pH value. As discussed earlier, pH critically influences the reaction pathways and the extent of side reactions. Therefore, controlling the local pH environment near the cathode has emerged as a simple yet powerful strategy. Wong et al. introduced 0.05 M sodium dihydrogen phosphate (NaH_2PO_4, SHP) as a pH buffer into $ZnSO_4$-based electrolytes, which suppressed vertical ZSH growth and mitigated MnO_2 dissolution.[76] With SHP additives, Zn–MnO_2 cells using electrodes with a mass loading of 8 mg cm^{-2} achieved a capacity retention of 83.3% over 1000 cycles at 1 A g^{-1} under a low N/P ratio of 2.24. Zhou et al. employed p-hydroxybenzaldehyde (M4) as an electrolyte additive to suppress proton-induced side reactions.[151] By stabilizing the local proton environment, M4 effectively enhanced the reversibility of the MnO_2/Mn^{2+} redox reaction, enabling a 1.68 Ah Zn–MnO_2 pouch cell to operate stably for over 100 cycles. Building on the concept of interfacial regulation, Zhou et al. introduced

a molecular additive, dioctyl phthalate (DOP), to form a stable CEI in situ during cycling.[91] The organic CEI effectively suppresses Mn dissolution and prevents the formation of inactive byproducts (Fig. 6d) and the high-loading Zn–MnO_2 pouch cell delivered a capacity of 2.5 Ah over 40 cycles (8 g Ah^{-1}).

4. Conclusion and perspectives

In this review, we provide a comprehensive overview of recent advances in Zn–MnO_2 batteries, with a particular focus on high-loading configurations as achieving high-loading MnO_2 cathodes is crucial for realizing the practical application of AZIBs in grid-scale energy storage (Fig. 7). While we realize its significance, we also outline the critical challenges, considering both the intrinsic material properties and reaction mechanisms of MnO_2, as well as the practical demands imposed by thick electrode architectures.

To address these challenges, we summarize the state-of-the-art design strategies for high-loading MnO_2 electrodes. Starting from the atomic level, lattice modifications, such as heteroatom doping, defect engineering, and superlattice construction, play vital roles in enhancing redox kinetics and mitigating structural degradation from Jahn–Teller distortion, thereby improving rate capability and cycling stability. Moving beyond atomic-scale design, surface coating strategies focus on regulating the local electrochemical environment of particles by introducing organic or inorganic layers. These coatings help stabilize the interfacial pH, effectively suppressing Mn dissolution and Mn^{3+} disproportionation.

At the macroscopic scale, substrate engineering and electrolyte optimization further improve the performance of thick MnO_2 electrodes. Tailoring the morphology, surface properties, and architecture of substrates promotes uniform MnO_2 deposition and efficient utilization of active materials. Meanwhile, the use of accelerators, redox mediators, and pH buffers in the electrolyte enables highly reversible, selective, and rapid redox reactions. Together, these multiscale design strategies pave the way for the development of high-performance, practical Zn–MnO_2 batteries for large-scale energy storage applications.

Despite the encouraging progress made in developing high-loading MnO_2 electrodes for practical Zn–MnO_2 batteries, significant efforts are still required to advance their real-world application. Finally, we would like to share our perspective on several potential research directions that warrant further exploration in the study of high-loading MnO_2 electrodes:

(1) To advance Zn–MnO_2 batteries from laboratory prototypes to practical energy storage systems, it is essential to establish industry-relevant performance benchmarks and define "high performance" under high-loading configurations. Target metrics should include a battery system cost ≤$50 per kWh, energy density ≥100 Wh kg^{-1} or ≥100 Wh L^{-1}, cycle life exceeding 1000 cycles, and robust operation under elevated temperatures and lean electrolyte conditions.[77,152,153] These criteria represent the requirements for competing with alterna-

tive battery chemistries—particularly for grid-scale and LDES applications—while aligning with the projected LCOS target of ≤\$0.05 per kWh.

(2) As discussed in section 2, poor electrochemical performance is intrinsically linked to the physicochemical characteristics of electrode architectures, including porosity, tortuosity, and effective ionic penetration depth. While the quantitative relationships between these parameters and electrochemical behavior have been widely established for many battery systems, comparable quantitative studies remain scarce for MnO_2 electrodes, particularly in the context of high areal capacity operation and the thick-electrode barrier. Developing systematic, quantitative analyses of these parameters would enable a unified framework for MnO_2 electrode design and provide clearer, more rational guidelines for developing thick MnO_2 electrodes suitable for practical implementation.

(3) Design strategies confined to a single length scale are often inadequate to tackle the practical and fundamental challenges of high-loading MnO_2 electrodes. Instead, synergistic multiscale approaches that integrate atomic-level lattice engineering, mesoscale surface coatings, and macroscale substrate and electrolyte optimization, would be essential for comprehensive performance improvements. In parallel, advanced characterization techniques beyond conventional X-ray diffraction and cyclic voltammetry, such as *operando* cryo-electron microscopy and hard X-ray methods, are crucial for capturing local, dynamic, and real-time processes across multiple length scales. These capabilities enable precise measurement of interfacial pH, direct visualization of the EDL, and monitoring of Mn valence states and structural evolution during cycling, thereby providing the mechanistic insights needed for the rational design of high-performance AZIBs.

(4) While recent studies have increasingly focused on achieving high areal loading and high energy density, the low-cost advantage—the defining requirement for practical Zn–MnO_2 batteries—must not be overlooked. It is worth noting that many reports demonstrating superior performance rely on modifications of lab-synthesized δ-MnO_2 or nanostructured materials, which undermines the intrinsic cost competitiveness of the Zn–MnO_2 system. Therefore, future efforts should prioritize developing high-performance electrodes built from low-cost, commercially available MnO_2 materials or implemented *via* an electrolysis configuration. Likewise, substrate and electrolyte designs should avoid expensive raw materials, complex synthesis routes, and processes that are difficult to scale. By balancing performance gains with cost constraints at every design level, the Zn–MnO_2 battery system can better realize its potential for truly low-cost, large-scale energy storage applications.

(5) To date, most studies have not demonstrated electrodes with mass loadings exceeding 5 mAh cm^{-2}, primarily due to manufacturing limitations. Overcoming this bottleneck will require optimized electrode fabrication strategies—for example, incorporating percolative carbon-based conductive networks and highly functionalized, flexible binders to preserve electrical connectivity and mechanical integrity at high

thickness. It is noteworthy that many recent studies achieving areal capacities above 10 mAh cm^{-2} have relied on electrolytic MnO_2 deposition directly onto conductive substrates, offering a promising alternative to conventional electrode fabrication routes. Moving forward, research efforts should focus on enhancing the reversibility and efficiency of cathodic reactions in electrolytic systems to enable practical, high-loading Zn–MnO_2 batteries.

Conflicts of interest

There are no conflicts to declare.

Data availability

No primary research results, software or code have been included and no new data was generated or analyzed as part of this review.

Acknowledgements

References

1 N. A. Sepulveda, J. D. Jenkins, A. Edington, D. S. Mallapragada and R. K. Lester, *Nat. Energy*, 2021, **6**, 506–516.

2 M. Staadecker, J. Szinai, P. A. Sánchez-Pérez, S. Kurtz and P. Hidalgo-Gonzalez, *Nat. Commun.*, 2024, **15**, 9501.

3 M. Li, J. Lu, Z. Chen and K. Amine, *Adv. Mater.*, 2018, **30**, 1800561.

4 J.-M. Tarascon and M. Armand, *Nature*, 2001, **414**, 359–367.

5 Y. Liang and Y. Yao, *Nat. Rev. Mater.*, 2023, **8**, 109–122.

6 Y. Xu, Z. Liu, X. Zheng, K. Li, M. Wang, W. Yu, H. Hu and W. Chen, *Adv. Energy Mater.*, 2022, **12**, 2103352.

7 G. Li, W. Chen, H. Zhang, Y. Gong, F. Shi, J. Wang, R. Zhang, G. Chen, Y. Jin, T. Wu, Z. Tang and Y. Cui, *Adv. Energy Mater.*, 2020, **10**, 1902085.

8 J. Yang, S. Bi, H. Wang, Y. Zhang, H. Yan and Z. Niu, *Angew. Chem., Int. Ed.*, 2024, **63**, e202409071.

9 H. Pan, Y. Shao, P. Yan, Y. Cheng, K. S. Han, Z. Nie, C. Wang, J. Yang, X. Li, P. Bhattacharya, K. T. Mueller and J. Liu, *Nat. Energy*, 2016, **1**, 16039.

10 R. Zhang, H. Xu, H. Dou and X. Zhang, *Adv. Funct. Mater.*, 2025, **35**, 2416497.

11 M. Li, S. Danitz, J. Holoubek, G. Cai, J. S. Lee, H. Zhang, W. Lu, J. Wu, X. Quinn, J. Truskier, S. Gorer, Y. S. Meng and Z. Chen, *Adv. Funct. Mater.*, 2025, **35**, 2508361.

12 M. H. Mostafa, S. H. E. Abdel Aleem, S. G. Ali, Z. M. Ali and A. Y. Abdelaziz, *J. Energy Storage*, 2020, **29**, 101345.

13 R. Yudhistira, D. Khatiwada and F. Sanchez, *J. Cleaner Prod.*, 2022, **358**, 131999.

14 J. Ye, L. Xia, H. Li, F. P. G. de Arquer and H. Wang, *Adv. Mater.*, 2024, **36**, 2402090.

15 G. Rodrigues, *Achieving the Promise of Low-Cost Long Duration Energy Storage*, U.S. Department of Energy, Office of Electricity, 2024.

16 V. Mathew, B. Sambandam, S. Kim, S. Kim, S. Park, S. Lee, M. H. Alfaruqi, V. Soundharrajan, S. Islam, D. Y. Putro, J.-Y. Hwang, Y.-K. Sun and J. Kim, *ACS Energy Lett.*, 2020, **5**, 2376–2400.

17 J. Luo, M. Cao, N. Naresh, J. Borah, S. Li, T. Wang, B. K. Sarma, J. Yao, I. P. Parkin and B. D. Boruah, *Adv. Funct. Mater.*, 2025, **35**, 2417607.

18 X. Li, Y. Xu, X. Chen, X. Yang, G. Zhang, X. Li and Q. Fu, *Adv. Sci.*, 2024, **11**, 2405134.

19 M. Li, M. Maisuradze, R. Sciacca, I. Hasa and M. Giorgetti, *Batteries Supercaps*, 2023, **6**, e202300340.

20 J. Peng, Y. Gao, H. Zhang, Z. Liu, W. Zhang, L. Li, Y. Qiao, W. Yang, J. Wang, S. Dou and S. Chou, *Angew. Chem.*, 2022, **134**, e202205867.

21 H. Zhang, J. Peng, L. Li, Y. Zhao, Y. Gao, J. Wang, Y. Cao, S. Dou and S. Chou, *Adv. Funct. Mater.*, 2023, **33**, 2210725.

22 Y. Zeng, J. Xu, Y. Wang, S. Li, D. Luan and X. W. (David) Lou, *Angew. Chem., Int. Ed.*, 2022, **61**, e202212031.

23 Y. Lyu, J. A. Yuwono, P. Wang, Y. Wang, F. Yang, S. Liu, S. Zhang, B. Wang, K. Davey, J. Mao and Z. Guo, *Angew. Chem.*, 2023, **135**, e202303011.

24 W. Du, Z. Song, X. Zheng, Y. Lv, L. Miao, L. Gan and M. Liu, *ChemSusChem*, 2024, **17**, e202400886.

25 J. Huang, Z. Wang, M. Hou, X. Dong, Y. Liu, Y. Wang and Y. Xia, *Nat. Commun.*, 2018, **9**, 2906.

26 N. Zhang, F. Cheng, J. Liu, L. Wang, X. Long, X. Liu, F. Li and J. Chen, *Nat. Commun.*, 2017, **8**, 405.

27 W. Sun, F. Wang, S. Hou, C. Yang, X. Fan, Z. Ma, T. Gao, F. Han, R. Hu, M. Zhu and C. Wang, *J. Am. Chem. Soc.*, 2017, **139**, 9775–9778.

28 W. Shi, W. S. V. Lee and J. Xue, *ChemSusChem*, 2021, **14**, 1634–1658.

29 M. Wang, Y. Meng, Y. Xu, N. Chen, M. Chuai, Y. Yuan, J. Sun, Z. Liu, X. Zheng, Z. Zhang, D. Li and W. Chen, *Energy Environ. Sci.*, 2023, **16**, 5284–5293.

30 X. Xiao, Z. Zhang, Y. Wu, J. Xu, X. Gao, R. Xu, W. Huang, Y. Ye, S. T. Oyakhire, P. Zhang, B. Chen, E. Cevik, S. M. Asiri, A. Bozkurt, K. Amine and Y. Cui, *Adv. Mater.*, 2023, **35**, 2211555.

31 Y. Yuan, R. Sharpe, K. He, C. Li, M. T. Saray, T. Liu, W. Yao, M. Cheng, H. Jin, S. Wang, K. Amine, R. Shahbazian-Yassar, M. S. Islam and J. Lu, *Nat. Sustainability*, 2022, **5**, 890–898.

32 C. Li, H. Yuan, T. Liu, R. Zhang, J. Zhu, H. Cui, Y. Wang, D. Cao, D. Wang and C. Zhi, *Angew. Chem.*, 2024, **136**, e202403504.

33 T. Xue and H. J. Fan, *J. Energy Chem.*, 2021, **54**, 194–201.

34 D. Chao, W. Zhou, F. Xie, C. Ye, H. Li, M. Jaroniec and S.-Z. Qiao, *Sci. Adv.*, 2020, **6**, eaba4098.

35 S. H. Kim and S. M. Oh, *J. Power Sources*, 1998, **72**, 150–158.

36 Y. Li, Y. Li, Q. Liu, Y. Liu, T. Wang, M. Cui, Y. Ding, H. Li and G. Yu, *Angew. Chem., Int. Ed.*, 2024, **63**, e202318444.

37 Q. Yang, X. Li, Z. Chen, Z. Huang and C. Zhi, *Acc. Mater. Res.*, 2022, **3**, 78–88.

38 X. Shen, X. Wang, Y. Zhou, Y. Shi, L. Zhao, H. Jin, J. Di and Q. Li, *Adv. Funct. Mater.*, 2021, **31**, 2101579.

39 A. Zhang, R. Zhao, Y. Wang, J. Yue, J. Yang, X. Wang, C. Wu and Y. Bai, *Angew. Chem., Int. Ed.*, 2023, **62**, e202313163.

40 Y. Huang, J. Mou, W. Liu, X. Wang, L. Dong, F. Kang and C. Xu, *Nano-Micro Lett.*, 2019, **11**, 49.

41 Y. Liao, H.-C. Chen, C. Yang, R. Liu, Z. Peng, H. Cao and K. Wang, *Energy Storage Mater.*, 2022, **44**, 508–516.

42 L. Wu, Z. Li, Y. Xiang, W. Dong, X. Qi, Z. Ling, Y. Xu, H. Wu, M. D. Levi, N. Shpigel and X. Zhang, *Small*, 2024, **20**, 2404583.

43 C. Zhao, M. Wu, W. Lu, Y. Cheng, X. Zhang, I. Saadoune, R. Lian, Y. Wang and Y. Wei, *Small*, 2024, **20**, 2401379.

44 S. Chen, Y. Kong, C. Tang, N. A. Gadelhak, A. K. Nanjundan, A. Du, C. Yu and X. Huang, *Small*, 2024, **20**, 2312229.

45 C. Zuo, F. Xiong, J. Wang, Y. An, L. Zhang and Q. An, *Adv. Funct. Mater.*, 2022, **32**, 2202975.

46 D. Chao, W. Zhou, C. Ye, Q. Zhang, Y. Chen, L. Gu, K. Davey and S.-Z. Qiao, *Angew. Chem.*, 2019, **131**, 7905–7910.

47 Q. Wang, Z. Liu, T. Xu, H. Li, Y. Chen and Y. Yan, *J. Power Sources*, 2024, **611**, 234763.

48 Q. Liu, L. Geng, T. Yang, Y. Tang, P. Jia, Y. Li, H. Li, T. Shen, L. Zhang and J. Huang, *Energy Storage Mater.*, 2019, **19**, 48–55.

49 J. Zhang, W. Li, J. Wang, X. Pu, G. Zhang, S. Wang, N. Wang and X. Li, *Angew. Chem.*, 2023, **135**, e202215654.

50 S. Cui, D. Zhang and Y. Gan, *Adv. Energy Mater.*, 2024, **14**, 2302655.

51 Y. Yuan, C. Liu, B. W. Byles, W. Yao, B. Song, M. Cheng, Z. Huang, K. Amine, E. Pomerantseva, R. Shahbazian-Yassar and J. Lu, *Joule*, 2019, **3**, 471–484.

52 Q. Zhang, J. Zhao, X. Chen, R. Yang, T. Ying, C. Cheng, B. Liu, J. Fan, S. Li and Z. Zeng, *Adv. Funct. Mater.*, 2024, **34**, 2306652.

53 S. Hong, S. Jin, Y. Deng, R. Garcia-Mendez, K. Kim, N. Utomo and L. A. Archer, *ACS Energy Lett.*, 2023, **8**, 1744–1751.

54 K. Shin, Y. Pei, X. Zhou, Q. Chen, P. Kidkhunthod, Y. Zheng, X. Guo, S. Tunmee, Q. Zhang and Y. Tang, *Adv. Mater.*, 2025, **37**, 2413645.

55 J. Xu, Q. Liu, Q. Yin, M. Tang, X. Huang, L. Shen and Y. Lu, *Small Methods*, 2025, 2500552.

56 S. Wu, H. Guo and C. Zhao, *Adv. Funct. Mater.*, 2024, **34**, 2405401.

57 F. Xiankai, X. Kaixiong, Z. Wei, D. Weina, Z. Hai, C. Liang and C. Han, *Carbon Energy*, 2024, **6**, e536.

58 J. Shin, J. K. Seo, R. Yaylian, A. Huang and Y. S. Meng, *Int. Mater. Rev.*, 2020, **65**, 356–387.

59 J. Ma, C. Li, Q. Ji, C. Liu, B. Tang, R. Liu, Y. Liu, N. Li, C. Wang, J. Zeng, K. Zheng and W. Yan, *Angew. Chem., Int. Ed.*, 2025, **64**, e202513148.

60 T. Hwang, M. Bergschneider, F. Kong and K. Cho, *Chem. Mater.*, 2025, **37**, 1244–1254.

61 M. H. Alfaruqi, S. Islam, V. Mathew, J. Song, S. Kim, D. P. Tung, J. Jo, S. Kim, J. P. Baboo, Z. Xiu and J. Kim, *Appl. Surf. Sci.*, 2017, **404**, 435–442.

62 G. G. Yadav, J. W. Gallaway, D. E. Turney, M. Nyce, J. Huang, X. Wei and S. Banerjee, *Nat. Commun.*, 2017, **8**, 14424.

63 B. Wu, G. Zhang, M. Yan, T. Xiong, P. He, L. He, X. Xu and L. Mai, *Small*, 2018, **14**, 1703850.

64 S. Gao, B. Li, K. Lu, S. Alabidun, F. Xia, C. Nickel, T. Xu and Y. Cheng, *ACS Appl. Mater. Interfaces*, 2021, **13**, 23724–23731.

65 Y. Ding, C. Cai, L. Ma, J. Wang, M. P. Mercer, J. Liu, D. Kramer, X. Yu, D. Xue, C. Zhi and C. Peng, *Adv. Energy Mater.*, 2025, **15**, 2402819.

66 W. Chen, G. Li, A. Pei, Y. Li, L. Liao, H. Wang, J. Wan, Z. Liang, G. Chen, H. Zhang, J. Wang and Y. Cui, *Nat. Energy*, 2018, **3**, 428–435.

67 D. Wu, L. M. Housel, S. J. Kim, N. Sadique, C. D. Quilty, L. Wu, R. Tappero, S. L. Nicholas, S. Ehrlich, Y. Zhu, A. C. Marschilok, E. S. Takeuchi, D. C. Bock and K. J. Takeuchi, *Energy Environ. Sci.*, 2020, **13**, 4322–4333.

68 D. Wu, S. T. King, N. Sadique, L. Ma, S. N. Ehrlich, S. Ghose, J. Bai, H. Zhong, S. Yan, D. C. Bock, E. S. Takeuchi, A. C. Marschilok, L. M. Housel, L. Wang and K. J. Takeuchi, *J. Mater. Chem. A*, 2023, **11**, 16279–16292.

69 Y. Liu, L. Lin, T. Zhang, Z. Xue, J. Liu, D. Chao and X. Sun, *Energy Environ. Sci.*, 2024, **17**, 2521–2529.

70 Y. Liu, K. Wang, X. Yang, J. Liu, X.-X. Liu and X. Sun, *ACS Nano*, 2023, **17**, 14792–14799.

71 H. Yang, T. Zhang, D. Chen, Y. Tan, W. Zhou, L. Li, W. Li, G. Li, W. Han, H. J. Fan and D. Chao, *Adv. Mater.*, 2023, **35**, 2300053.

72 C. F. Bischoff, O. S. Fitz, J. Burns, M. Bauer, H. Gentischer, K. P. Birke, H.-M. Henning and D. Biro, *J. Electrochem. Soc.*, 2020, **167**, 020545.

73 O. Fitz, C. Bischoff, M. Bauer, H. Gentischer, K. P. Birke, H.-M. Henning and D. Biro, *ChemElectroChem*, 2021, **8**, 3553–3566.

74 J. M. Mayer, *J. Am. Chem. Soc.*, 2023, **145**, 7050–7064.

75 X. Ye, D. Han, G. Jiang, C. Cui, Y. Guo, Y. Wang, Z. Zhang, Z. Weng and Q.-H. Yang, *Energy Environ. Sci.*, 2023, **16**, 1016–1023.

76 M. Chen, M. Yang, X. Han, J. Chen, P. Zhang and C.-P. Wong, *Adv. Mater.*, 2024, **36**, 2304997.

77 M. B. Lim and T. N. Lambert, *Rechargeable Zinc Batteries for Grid Storage*, Sandia National Laboratories, DOE Office of Electricity, 2021, ch. 5.

78 J. S. Newman and C. W. Tobias, *J. Electrochem. Soc.*, 1962, **109**, 1183.

79 K. G. Gallagher, S. E. Trask, C. Bauer, T. Woehrle, S. F. Lux, M. Tschech, P. Lamp, B. J. Polzin, S. Ha, B. Long, Q. Wu, W. Lu, D. W. Dees and A. N. Jansen, *J. Electrochem. Soc.*, 2015, **163**, A138.

80 M. Doyle, J. Newman, A. S. Gozdz, C. N. Schmutz and J.-M. Tarascon, *J. Electrochem. Soc.*, 1996, **143**, 1890.

81 J.-H. Kim, N.-Y. Kim, Z. Ju, Y.-K. Hong, K.-D. Kang, J.-H. Pang, S.-J. Lee, S.-S. Chae, M.-S. Park, J.-Y. Kim, G. Yu and S.-Y. Lee, *Nat. Energy*, 2025, **10**, 295–307.

82 H. Kim, S. K. Oh, J. Lee, S. W. Doo, Y. Kim and K. T. Lee, *Electrochim. Acta*, 2021, **370**, 137743.

83 S. J. Tambio, F. Cadiou, E. Maire, N. Besnard, M. Deschamps and B. Lestriez, *J. Electrochem. Soc.*, 2020, **167**, 160509.

84 M. White, M. Choi, B. Hu, S. Chandrasekaran, X. Xue, M. Worsley, Y. Li and B. Dunn, *Adv. Mater.*, 2025, **37**, 2417128.

85 J. Zheng, G. Xing, L. Jin, Y. Lu, N. Qin, S. Gao and J. P. Zheng, *Batteries*, 2023, **9**, 151.

86 M. Mateos, N. Makivic, Y.-S. Kim, B. Limoges and V. Balland, *Adv. Energy Mater.*, 2020, **10**, 2000332.

87 Y. Liu, C. Xie and X. Li, *Small*, 2024, **20**, 2402026.

88 A. F. Routh and W. B. Zimmerman, *Chem. Eng. Sci.*, 2004, **59**, 2961–2968.

89 J. Zhou, X. Man, Y. Jiang and M. Doi, *Adv. Mater.*, 2017, **29**, 1703769.

90 K. B. Singh and M. S. Tirumkudulu, *Phys. Rev. Lett.*, 2007, **98**, 218302.

91 G. Lai, Z. Zhao, H. Zhang, X. Hu, B. Lu, S. Liang and J. Zhou, *Nat. Commun.*, 2025, **16**, 2194.

92 S. Mubarak, D. Dhamodharan and H.-S. Byun, *J. Energy Chem.*, 2023, **81**, 272–312.

93 N. Nie, F. Wang and W. Yao, *Electrochim. Acta*, 2023, **472**, 143423.

94 Y. Li, X. Zheng, E. Z. Carlson, X. Xiao, X. Chi, Y. Cui, L. C. Greenburg, G. Zhang, E. Zhang, C. Liu, Y. Yang, M. S. Kim, G. Feng, P. Zhang, H. Su, X. Guan, J. Zhou, Y. Wu, Z. Xue, W. Li, M. Bajdich and Y. Cui, *Nat. Energy*, 2024, **9**, 1350–1359.

95 H. Yang, Y. Wan, K. Sun, M. Zhang, C. Wang, Z. He, Q. Li, N. Wang, Y. Zhang, H. Hu and M. Wu, *Adv. Funct. Mater.*, 2023, **33**, 2215076.

96 Q. Zhao, A. Song, S. Ding, R. Qin, Y. Cui, S. Li and F. Pan, *Adv. Mater.*, 2020, **32**, 2002450.

97 J.-J. Ye, P.-H. Li, Z. Hou, W. Zhang, W. Zhu, S. Jin and H. Ji, *Angew. Chem.*, 2024, **136**, e202410900.

98 N. Jiang, Y. Zeng, Q. Yang, P. Lu, K. Qu, L. Ye, X. Lu, Z. Liu, X. Li, Y. Tang, J. Cao, S. Chen, C. Zhi and J. Qiu, *Energy Environ. Sci.*, 2024, **17**, 8904–8914.

99 T. Xiong, Z. G. Yu, H. Wu, Y. Du, Q. Xie, J. Chen, Y.-W. Zhang, S. J. Pennycook, W. S. V. Lee and J. Xue, *Adv. Energy Mater.*, 2019, **9**, 1803815.

100 S. Ding, M. Zhang, R. Qin, J. Fang, H. Ren, H. Yi, L. Liu, W. Zhao, Y. Li, L. Yao, S. Li, Q. Zhao and F. Pan, *Nano-Micro Lett.*, 2021, **13**, 173.

101 Y. Zhao, P. Zhang, J. Liang, X. Xia, L. Ren, L. Song, W. Liu and X. Sun, *Energy Storage Mater.*, 2022, **47**, 424–433.

102 J. Liang, Y. Zhao, L. Ren, M. Li, Q. Zhang, Y. Wang, X. Sun, M. Chuai, X. Wang and W. Liu, *Adv. Funct. Mater.*, 2025, **35**, 2501135.

103 S. Wang, S. Yao, N. Dai, W. Fu, Y. Liu, K. Ji, Y. Ji, J. Yang, R. Liu, X. Li, J. Xie, Z. Yang and Y.-M. Yan, *Angew. Chem., Int. Ed.*, 2024, **63**, e202408414.

104 Y. Chen, C. Lin, X. Chen, Z. Lu, K. Zhang, Y. Liu, J. Wang, G. Han and G. Xu, *Adv. Energy Mater.*, 2024, **14**, 2304303.

105 X. Liang, X. Liu, P. Wang, Z. Guo, X. Chen, J. Yao, J. Li, Y. Gan, L. Lv, L. Tao, H. Wang, H. Wan, J. Zhang and H. Wang, *J. Power Sources*, 2025, **635**, 236518.

106 Z. Wang, K. Han, Q. Wan, Y. Fang, X. Qu and P. Li, *ACS Appl. Mater. Interfaces*, 2023, **15**, 859–869.

107 J. Xia, Y. Zhou, J. Zhang, T. Lu, W. Gong, D. Zhang, X. Wang and J. Di, *Small*, 2023, **19**, 2301906.

108 T. Li, N. Zhang, B. Liu, P. Wang, Z. Liu, Y. Wang, D. Xu, H. Tian, Q. Zhang and T.-F. Yi, *Adv. Funct. Mater.*, 2025, **35**, 2423755.

109 T. Wang, J. Jin, X. Zhao, X. Qu, L. Jiao and Y. Liu, *Angew. Chem.*, 2024, **136**, e202412057.

110 S. Yang, F. Li, P. Fu, C. Zhen, J. Wu, Y. Feng, H. Lu and Z. Sheng, *J. Power Sources*, 2024, **611**, 234767.

111 F. W. Fenta, B. W. Olbasa, M.-C. Tsai, N. T. Temesgen, W.-H. Huang, T. M. Tekaligne, Y. Nikodimos, S. Wu, W.-N. Su, H. Dai and B. J. Hwang, *J. Power Sources*, 2022, **548**, 232010.

112 B. Zhang, J. Chen, W. Sun, Y. Shao, L. Zhang and K. Zhao, *Energies*, 2022, **15**, 4698.

113 X. Gao, C. Shen, H. Dong, Y. Dai, P. Jiang, I. P. Parkin, H. Zhang, C. J. Carmalt and G. He, *Energy Environ. Sci.*, 2024, **17**, 2287–2297.

114 Y. Wang, Y. Zhang, G. Gao, Y. Fan, R. Wang, J. Feng, L. Yang, A. Meng, J. Zhao and Z. Li, *Nano-Micro Lett.*, 2023, **15**, 219.

115 J. Wu, F. Huang, T. Lee, Y. Yan, X. Pei, M. Wang, S. Gao, S. Guo, X. Pan and P. Wang, *ACS Appl. Energy Mater.*, 2022, **5**, 6962–6969.

116 M. Jiang, C. Fu, J. Yang, Q. Liu, J. Zhang and B. Sun, *Energy Storage Mater.*, 2019, **18**, 34–42.

117 W. Lv, J. Meng, J. Li, W. Yang, Y. Tian, X. Lyu, C. Duan, X. Ma and Y. Wu, *Nano Energy*, 2022, **98**, 107274.

118 S. Wang, X. Guo, K. Huang, A. Achari, J. Safaei, Y. Lei, D. Li, Q. Gu, C. Sun, L. Gloag, S. Langford, A. Geim, R. R. Nair and G. Wang, *Nat. Commun.*, 2025, **16**, 5191.

119 A. Zhang, T. Chen, R. Zhao, Y. Wang, J. Yang, X. Han, X. Wang, C. Wu and Y. Bai, *Angew. Chem., Int. Ed.*, 2025, **64**, e202423824.

120 W. J. Kim, M. A. Smeaton, C. Jia, B. H. Goodge, B.-G. Cho, K. Lee, M. Osada, D. Jost, A. V. Ievlev, B. Moritz, L. F. Kourkoutis, T. P. Devereaux and H. Y. Hwang, *Nature*, 2023, **615**, 237–243.

121 C. Zuo, F. Chao, M. Li, Y. Dai, J. Wang, F. Xiong, Y. Jiang and Q. An, *Adv. Energy Mater.*, 2023, **13**, 2301014.

122 T. Zhang, T. Li, Y. Shen, H. Ma, C. Wei, J. Cai, Y. Xu, Y. Li, X. Dong, S. Zhang, F. Huang and T. Lin, *Adv. Mater.*, 2025, **37**, 2505082.

123 G. Lai, X. Hu, S. Liang, Y. Yang, E. R. Elsharkawy, G. A. M. Mersal, B. Lu, Z. M. El-Bahy, Y. Liu and J. Zhou, *ACS Energy Lett.*, 2025, **10**, 3437–3444.

124 X. Xiao, L. Zhang, W. Xin, M. Yang, Y. Geng, M. Niu, H. Zhang and Z. Zhu, *Small*, 2024, **20**, 2309271.

125 S. Paik, I. Choi, S. Lee and K. W. Nam, *ACS Appl. Mater. Interfaces*, 2024, **16**, 50775–50784.

126 Q. Li, M. Xu, S. Wei, A. Kumar, K. K. Abdalla, Y. Wang, L. Yu, M. Liu, X. Jin, J. Li, L. Song, Y. Zhao and X. Sun, *Energy Environ. Sci.*, 2025, **18**, 7939–7949.

127 Y. Xu, G. Zhang, J. Liu, J. Zhang, X. Wang, X. Pu, J. Wang, C. Yan, Y. Cao, H. Yang, W. Li and X. Li, *Energy Environ. Mater.*, 2023, **6**, e12575.

128 D. Lin, S. Chandrasekaran, J.-B. Forien, X. Xue, A. Pinongcos, E. Coester, M. A. Worsley and Y. Li, *Adv. Energy Mater.*, 2023, **13**, 2300408.

129 B. Yao, S. Chandrasekaran, J. Zhang, W. Xiao, F. Qian, C. Zhu, E. B. Duoss, C. M. Spadaccini, M. A. Worsley and Y. Li, *Joule*, 2019, **3**, 459–470.

130 P. De and M. Pumera, *Small*, 2024, **20**, 2404227.

131 F. Wu, X. Gao, X. Xu, Y. Jiang, X. Gao, R. Yin, W. Shi, W. Liu, G. Lu and X. Cao, *ChemSusChem*, 2020, **13**, 1537–1545.

132 J. Shi, S. Wang, Q. Wang, X. Chen, X. Du, M. Wang, Y. Zhao, C. Dong, L. Ruan and W. Zeng, *J. Power Sources*, 2020, **446**, 227345.

133 X. Zheng, Y. Wang, Y. Xu, T. Ahmad, Y. Yuan, J. Sun, R. Luo, M. Wang, M. Chuai, N. Chen, T. Jiang, S. Liu and W. Chen, *Nano Lett.*, 2021, **21**, 8863–8871.

134 Y. Cai, L. Sun, Z. Chen, Y. Zhang, H. Morikawa and C. Zhu, *Electrochim. Acta*, 2025, **509**, 145297.

135 Y. Ren, F. Meng, S. Zhang, B. Ping, H. Li, B. Yin and T. Ma, *Carbon Energy*, 2022, **4**, 446–457.

136 M. R. Panda, S. El Meragawi, M. S. Mirshekarloo, W. Chen, M. Shaibani and M. Majumder, *Small*, 2025, **21**, 2311933.

137 Y. Zhao, R. Zhou, Z. Song, X. Zhang, T. Zhang, A. Zhou, F. Wu, R. Chen and L. Li, *Angew. Chem., Int. Ed.*, 2022, **61**, e202212231.

138 Y. Qi, F. Li, H. Sheng, H. Zhang, J. Yuan, L. Ma, H. Bi, Y. Ma, W. Li and W. Lan, *Small*, 2024, **20**, 2404312.

139 L. Gou, J. Li, K. Liang, S. Zhao, D. Li and X. Fan, *Small*, 2023, **19**, 2208233.

140 J. Li, X. Yang, J. Wang, C. Ma, T. Wang, N. Liu, X. Pang, Q. Zhang, C. Wu and X. Li, *Energy Storage Mater.*, 2025, **74**, 103887.

141 Q. Chen, J. Li, C. Liao, W. Liang, X. Lou, Z. Liu, J. Zhang, Y. Tang, L. Mai, L. Zhou and K. Amine, *Nano Energy*, 2024, **126**, 109607.

142 H. Qiao, H. Zhu, X. Li, Y. Wang, C. Ye, L. Ma, J. Shen and M. Ye, *Adv. Energy Mater.*, 2024, **14**, 2304357.

143 C. Li, B. Liang, Z. Chen, R. Zhang, H. Cui, Y. Wang, Q. Li, C. Peng, J. Fan, Z. Pei and C. Zhi, *Proc. Natl. Acad. Sci. U. S. A.*, 2025, **122**, e2501935122.

144 H. Li, S. Wang, Z. Feng, Z. Liu, Y. Liu, M. Yang, P. Gao, L. Fu and X. Zhao, *Adv. Mater.*, 2025, **37**, e14328.

145 M. Chuai, J. Yang, R. Tan, Z. Liu, Y. Yuan, Y. Xu, J. Sun, M. Wang, X. Zheng, N. Chen and W. Chen, *Adv. Mater.*, 2022, **34**, 2203249.

146 M. Chuai, H. Tong, Z. Yang, S. Deng, M. Wu, J. Xing and G. Chai, *J. Am. Chem. Soc.*, 2025, **147**, 31591–31602.

147 Y. Liu, Z. Qin, X. Yang, J. Liu, X.-X. Liu and X. Sun, *ACS Energy Lett.*, 2022, **7**, 1814–1819.

148 S. Gao, B. Li, H. Tan, F. Xia, O. Dahunsi, W. Xu, Y. Liu, R. Wang and Y. Cheng, *Adv. Mater.*, 2022, **34**, 2201510.

149 W. Fan, S. Tian, L. Qin, T. S. Alomar, P. Ruan, Z. M. El-Bahy, N. AlMasoud, B. Lu and J. Zhou, *J. Am. Chem. Soc.*, 2025, **147**, 18694–18703.

150 X. Xue, Z. Liu, S. Chandrasekaran, S. Eisenberg, C. Althaus, M. C. Freyman, A. Pinongcos, Q. Ren, L. Valdovinos, C. Hsieh, B. Hu, B. Dunn, C. A. Orme, X. Wang, M. A. Worsley and Y. Li, *Adv. Mater.*, 2025, **37**, 2419505.

151 Y. Liu, Z. Liu, Z. Xiao, Z. Lao, J. Liu, X. Xiao, Q. Fu, F. Zheng and G. Zhou, *Angew. Chem., Int. Ed.*, 2025, **64**, e202502896.

152 A. Poullikkas, *Renewable Sustainable Energy Rev.*, 2013, **27**, 778–788.

153 E. D. Spoerke, H. Passell, G. Cowles, T. N. Lambert, G. G. Yadav, J. Huang, S. Banerjee and B. Chalamala, *MRS Energy Sustainability*, 2022, **9**, 13–18.